

Analysis of a Quadrotor in Forward Flight

by

James Neil Wiken

B.S., Aeronautical Engineering with Information Technology
Massachusetts Institute of Technology (2013)

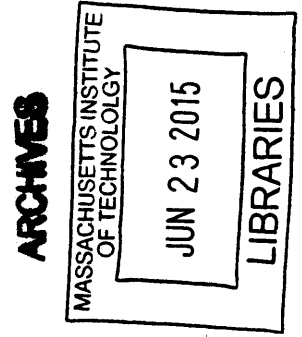
Submitted to the Department of Aeronautics and Astronautics
in partial fulfillment of the requirements for the degree of
Masters of Science in Aeronautics and Astronautics

at the

MASSACHUSETTS INSTITUTE OF TECHNOLOGY

June 2015

© Massachusetts Institute of Technology 2015. All rights reserved.



Author **Signature redacted**
Department of Aeronautics and Astronautics
May 21, 2015

Certified by **Signature redacted**
Jonathan P. How
Richard C. Maclaurin Professor of Aeronautics and Astronautics
Thesis Supervisor

Accepted by **Signature redacted**
Paulo C. Lozano
Associate Professor of Aeronautics and Astronautics
Chairman, Department Committee on Graduate Theses

Analysis of a Quadrotor in Forward Flight

by

James Neil Wiken

Submitted to the Department of Aeronautics and Astronautics
on May 21, 2015, in partial fulfillment of the
requirements for the degree of
Masters of Science in Aeronautics and Astronautics

Abstract

In general, quadrotors are designed to be stabilized about hover conditions. This allows the dynamics of the vehicle to be linearized about a single equilibrium point. Additionally, aerodynamic effects can be neglected leaving only rigid body dynamics to be modeled. While this formulation works under hover conditions, it is no longer valid when flying at high speed or in prolonged forward flight as the aerodynamics can no longer be ignored. This results in a highly nonlinear system with both aerodynamics and rigid body dynamics affecting the dynamics.

In this thesis, a model of a quadrotor that takes into account both rigid-body dynamics and aerodynamics is presented. Flight testing was performed to test the validity of the this dynamic model. These flight tests were performed using a new flight space integrated into the Wright Brothers Wind Tunnel using a motion capture system. Additional flight tests were performed to gather data for a system identification of a quadrotor in forward flight using subspace methods. The results of the system identification can be used for control design for the system.

Thesis Supervisor: Jonathan P. How

Title: Richard C. Maclaurin Professor of Aeronautics and Astronautics

Acknowledgments

First, I would like to thank my adviser, Professor Jonathan How. His patience and guidance have helped me through graduate school. He has an impressive ability of being able to get to the root a complex problem to find the solution.

I would also like to thank Professor Sheila Widnall for giving me the opportunity to assist with teaching Dynamics. This was one of my most fulfilling opportunities while at MIT. Also thanks to Professor Julie Shah, her mentoring over the past five years has helped me during my entire MIT career.

I would also like to extend my gratitude to Richard Perdichizzi and David Robertson for their assistance with setting up, troubleshooting, and operating the new flight space added to the Wright Brothers Wind Tunnel.

Finally I would like to thank my all the members of the Aerospace Controls Laboratory. Much of what I have learned and accomplished over the past two years is because of those around me. In particular I would like to thank Mark Cutler for not only developing much of the hardware and software used to complete my research but to always be willing to answer any questions or help solve any problem I ran into. Also thanks to Brett Lopez, Byron Patterson, Justin Miller, John Quindlen, and Michael Klinker for assistance with flight testing and providing a sounding board to work through research problems.

This thesis is based upon work supported by the “Predictive Modeling in Uncertain Environments for Threat Assessment and Autonomous Driving” project under the Ford-MIT Alliance Agreement January 2008.

Contents

1	Introduction	13
1.1	Motivation	13
1.2	Literature Review	14
1.3	Contributions	15
2	Dynamics in Forward Flight	17
2.1	Rigid Body Dynamics	17
2.2	Aerodynamic Effects	20
2.2.1	Aerodynamic Drag	21
2.2.2	Induced Thrust	22
2.2.3	Blade Flapping	23
2.3	Equations of Motion	25
3	System Architecture and Control	27
3.1	System Architecture	27
3.2	Feedback Control	28
3.2.1	Position Control	30
3.2.2	Attitude Control	34
3.3	System Dynamics	36
3.4	Simulation Results	37
3.4.1	Steady State Attitude Response	40
3.4.2	Actuation Limits	40
3.4.3	Control Performance	42

3.5	Summary	46
4	Flight Space	47
4.1	Wind Tunnel	48
4.2	Camera Placement	49
4.3	Vehicle Setup	51
5	Hardware and Software Implementation	55
5.1	Aircraft	55
5.1.1	Physical Parameters	55
5.1.2	Aerodynamic Properties	56
5.2	Software	58
5.2.1	Outer Loop	59
5.2.2	Inner Loop	60
5.2.3	Data Logging	60
5.3	Summary	60
6	Experimental Results	63
6.1	Experimental Design	63
6.2	Comparison of Physical and Simulated System	64
6.3	System Identification	66
6.4	Model for Quadrotor in Forward Flight	69
6.5	Summary	73
7	Conclusion	75
7.1	Summary	75
7.2	Future Work	77
A	Wright Brothers Wind Tunnel Flight Space Operation Manual	79
A.1	System Setup	79
A.2	System Operation	81

List of Figures

2-1	Free Body Diagram of a Quadrotor in Hover Conditions with Body Reference Frame B Centered at Q and Inertial Reference Frame I Centered at O	18
2-2	Free Body Diagram of a Quadrotor in Forward Flight with Body Reference Frame B Centered at Q and Inertial Reference Frame I Centered at O	21
2-3	Blade Flap Angle of the Rotor Due to a Relative Wind [1]	24
3-1	Top Level Block Diagram of the Simulated System	28
3-2	Top Level Simulink Diagram of Simulated System	29
3-3	Simulink Diagrams of Blocks "positionController"; "positionController/getAccel", and "positionControl/getAtt"	31
3-4	Simulink Diagram of Block "attitudeController". This Block Corresponds to the Attitude Control Loop (Inner Control Loop Described in Section 3.2.2	35
3-5	Simulink Diagram of Block "equations of motion" Corresponds to the System Dynamics Described in Section 3.3	38
3-6	Simulink Diagram of Block "equations of motion/6DOF (Quaternion)"	39
3-7	Steady State Pitch of the Simulated System as a Function of Wind Speed	41
3-8	System Response of Simulated Quadrotor Above Maximum Operating Speed (32 mph). From Top to Bottom, The Plots Show Velocity in the Inertial Frame, Position in the Inertial Frame, Attitude in Euler Angles, and the Induced Thrust Forces All With Respect To Time.	42

3-9	System Response of Simulated Quadrotor at Maximum Operating Speed (30 mph) From Top to Bottom, The Plots Show Velocity in the Inertial Frame, Position in the Inertial Frame, Attitude in Euler Angles, and the Induced Thrust Forces All With Respect To Time.	43
3-10	System Response Time as a Function of Wind Speed	45
3-11	Tracking Reference Sine Wave in X-Position at 9 m/s (20 mph)	45
4-1	Wright Brothers Wind Tunnel Flight Space with Vicon System	47
4-2	Wright Brothers Wind Tunnel Diagram [2]	48
4-3	Vicon Camera Placement in Wright Brothers Wind Tunnel	50
4-4	Flight Vehicle Size Reference	52
4-5	Example Vicon Dot Arrangement	53
5-1	The BuddyQuad, a Quadrotor Designed at the Aerospace Controls Lab	56
6-1	Steady State Pitch of the Simulated and Physical Systems as a Function of Wind Speed	65
6-2	Model Output of Single State-Space System Identification Compared to Validation Data at 25 mph (11.2 m/s)	70
6-3	Model Output for Estimated Pitch Compared to Validation Data at 20 mph (9 m/s)	73
6-4	Model Output of 4th Order, 4 Input State-Space System Identification Compared to Validation Data at 25 mph (11.2 m/s)	74
A-1	Wright Brothers Wind Tunnel Flight Space with Vicon System	80
A-2	Components of the Vicon system in the Wright Brothers Wind Tunnel	81
A-3	Network Setup for Flight Space	82
A-4	Vicon Camera Placement in Wright Brothers Wind Tunnel	83
A-5	Example Tripod Setup Within Test Section	84
A-6	Vicon System Calibration Tools	85
A-7	Set Volume Origin Example (Camera Facing Upwind)	87

List of Tables

3.1	Rise and Settling Time of the Simulated System at High Speed	44
5.1	Physical Parameters of BuddyQuad	57
5.2	Aerodynamic Properties of BuddyQuad	59
6.1	Total Error of Model Output Compared to Validation Data	71

Chapter 1

Introduction

1.1 Motivation

Over the past decade or so, quadrotors have become an increasingly common type of aircraft in the field of unmanned aerial vehicles. They are used in an increasingly wide area of research topics ranging from forest fire observation [3] to package delivery[4]. As the range of quadrotor applications expands, so does the range of domains they must fly in, pushing into more extreme flight conditions. Recently, a particular interest in sustained high-speed quadrotor flight has increased [5].

High-speed flight, or forward flight, is an interesting regime for quadrotors as aerodynamic effects that are typically ignored when modeling these aircraft become increasingly important to the overall dynamics of the system as the speed of the aircraft increases. In forward flight, assumptions made about hover conditions, common in linear control techniques for quadrotors, become invalid as the aircraft is consistently operating at non-zero attitude conditions.

This thesis explores the difference in dynamics of a quadrotor when flying at high speeds compared to one operating about hover conditions. The dynamics model for the quadrotor must be augmented with aerodynamic effects which are commonly neglected in modeling multirotor aircraft. The aerodynamic effects govern the steady state response of the system when flying at a constant forward speed.

This thesis focuses on using experimental data to drive the analysis of the system.

Flight tests were performed with a quadrotor in forward flight at nearly 30 mph. To perform these flight tests, a new flight space capable of supporting sustained high speed flight was developed.

1.2 Literature Review

Small quadrotors, first developed as recreational electronic aircraft, gained popularity as platforms for aerial control in the early 2000s [6]. In the past decade, they have become increasingly common as test aircraft for controls research. In addition to the mechanical simplicity and relatively low cost of the aircraft, low speed quadrotor flight is well understood and highly documented.

Early works in quadrotor flight and control often approximated the dynamics of the aircraft into a linear system [7]. This allowed the system to be controlled by a simple linear controller, often around hover conditions. More recently, nonlinear control techniques have been applied to nonlinear models of quadrotors [8] [9]. These models, however, neglect the aerodynamic effects acting on the vehicle which become relevant while flying at high speeds. When flying in demanding flight regimes such as these, the control performance can be diminished if the aerodynamic effects are neglected [10]. In these situations, the control signals could drive the system into the region of saturation causing undesirable or even unstable behavior. These effects are especially important to model when the quadrotor is flying near its operational limits [11].

More recently, there has been some work on incorporating aerodynamic effects into quadrotor models. [10] discusses the effects of blade flapping and induced thrust acting on a quadrotor. The behavior of a quadrotor propulsion system (with focus on its limitations) while in forward or descent flight is discussed in [11]. A six degree-of-freedom model incorporating blade flapping, induced thrust, and aerodynamic drag is presented in [1]. However, both [11] and [1] only provide simulation data based on their models. [10] provides some experimental data to specifically model blade flapping, but is largely limited to test stand flights.

1.3 Contributions

The main contributions of this thesis are as follows:

1. A new flight space is constructed by augmenting a wind tunnel with a motion capture system to allow for autonomous free flight at high forward speeds. Additionally, an operation manual for the flight space is provided.
2. The validity of a full dynamic model incorporating rigid body dynamics and aerodynamic effects is evaluated using flight test data.
3. Flight experiments are conducted to perform a system identification of a quadrotor in forward flight, providing estimated state-space models for the system at different flight speeds.

Chapter 2 provides the derivation of a dynamic model for a quadrotor in sustained forward flight. This model incorporates both the rigid-body dynamics commonly model in quadrotor dynamics and aerodynamic effects that become important when flying at high speed.

A system architecture including controller formulation is provided for the system in Chapter 3. The control law presented is not based on near-hover conditions, which makes it usable for the flight regime being analyzed. Additionally, the full system is simulated using Simulink, the implementation of which is detailed. Steady state performance, operating limits, and control performance of the system are then discussed.

Chapter 4 details the design of the new flight space in the Wright Brothers Wind Tunnel. The properties and capabilities of the wind tunnel are briefly overviewed. The design and reasoning behind the camera placement is then discussed. Finally, vehicle setup and limitations while flying in the wind tunnel are provided.

The hardware and software implementation of the flight tests is detailed in Chapter 5. Included are tables of the physical and aerodynamic qualities of the test aircraft. The flight software and control implementation is also discussed.

Experimental results from flight tests performed in the wind tunnel flight space are presented and analyzed in Chapter 6. The experimental design and challenges are discussed. A comparison of the simulated system from Chapter 3 and the performance of the physical system is discussed. A brief overview of subspace methods for system identification of state-space systems is given. The system identification process is described along with performance results of the final state-space model of the quadrotor in forward flight at various speeds.

Concluding remarks and suggestions for future work are given in Chapter 7.

Chapter 2

Dynamics in Forward Flight

In this chapter, the dynamics of a quadrotor in forward flight are derived. This model is complicated by the fact that a quadrotor flying at sustained high speeds is subject to both the high speed body dynamics (normally experienced by quadrotors in hover conditions) and the low speed aerodynamic effects more commonly seen in fixed-wing aircraft. This combination of effects results in a highly nonlinear set of equations of motion.

The chapter begins with a review of the rigid body dynamics used to model quadrotors at hover conditions in Section 2.1. Section 2.2 discusses the various aerodynamic effects that a quadrotor experiences while operating in forward flight and how they are incorporated into the existing dynamic models. Finally, Section 2.3 is the complete equations of motion for a quadrotor in forward flight.

2.1 Rigid Body Dynamics

This section derives the equations of motion for a quadrotor in hover conditions. The free-body diagram shown in Figure 2-1 shows the forces acting on the quadrotor in hover conditions and the two reference frames used through the rest of the thesis. This includes the inertial reference frame I (centered at origin O , unit vectors $\mathbf{i}_x, \mathbf{i}_y, \mathbf{i}_z$) and the body reference frame B (centered at origin Q , unit vectors $\mathbf{b}_x, \mathbf{b}_y, \mathbf{b}_z$). Five forces act on the quadrotor in hover conditions: gravity and the four thrust forces.

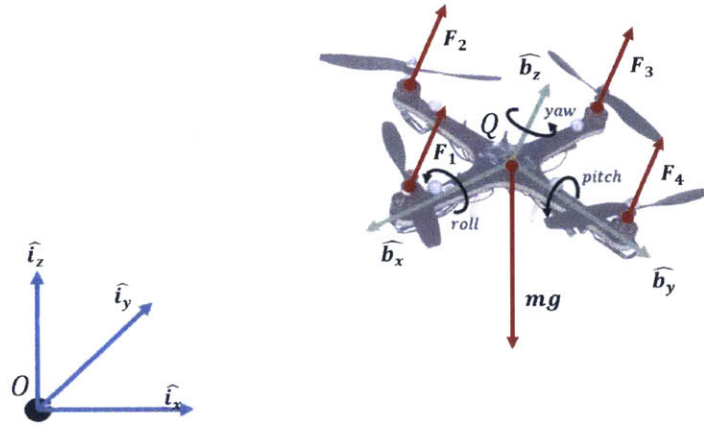


Figure 2-1: Free Body Diagram of a Quadrotor in Hover Conditions with Body Reference Frame B Centered at Q and Inertial Reference Frame I Centered at O

The inertial orientation of the body frame is described using a 3-2-1 Euler angle sequence (yaw (ψ), pitch (θ), then roll (ϕ)). The transformation matrix from the body frame to the inertial frame is

$${}^I R^B = \begin{bmatrix} c\theta c\psi & s\phi s\theta c\psi - c\phi s\psi & c\phi s\theta c\psi + s\phi s\psi \\ c\theta s\psi & s\phi s\theta s\psi + c\phi c\psi & c\phi s\theta s\psi + s\phi c\psi \\ -s\theta & s\phi c\theta & c\phi c\theta \end{bmatrix} \quad (2.1)$$

where $c\theta$ and $s\theta$ are abbreviations for $\cos\theta$ and $\sin\theta$, respectively. This also applies for the other angles, ϕ and ψ .

Derivation of the translational equations of motion starts with Newton's 2nd Law

$$\sum \vec{F} = m\vec{a}. \quad (2.2)$$

As stated above, there are five forces acting on the aircraft: gravity (mg) and the four motor thrusts (F_1, F_2, F_3, F_4). Gravity always points purely in the negative \mathbf{i}_z direction. The four thrust forces all point purely in the \mathbf{b}_z direction. Using this knowledge and Equation 2.1, Newton's 2nd Law can be rewritten into translational

equations of motion for the quadrotor

$$m \begin{bmatrix} \ddot{x} \\ \ddot{y} \\ \ddot{z} \end{bmatrix} = {}^I R^B \begin{bmatrix} 0 \\ 0 \\ F_{total} \end{bmatrix}_B - \begin{bmatrix} 0 \\ 0 \\ mg \end{bmatrix}_I \quad (2.3)$$

where F_{total} is the sum of the thrust forces, m is the mass of the aircraft, and $\begin{bmatrix} \ddot{x} & \ddot{y} & \ddot{z} \end{bmatrix}^T$ is the second derivative of the position vector of the quadrotor in the inertial frame (\mathbf{p})

$$\mathbf{p} = x\mathbf{i}_x + y\mathbf{i}_y + z\mathbf{i}_z. \quad (2.4)$$

The rotational equations of motion are derived from the rotational equivalent of Newton's 2nd Law

$$\sum \tau = I\dot{\omega}$$

where τ is a torque, I is the inertia tensor, and $\dot{\omega}$ is the time derivative of the angular velocity of the quadrotor body frame with respect to the inertial frame

$$\omega = p\mathbf{b}_x + q\mathbf{b}_y + r\mathbf{b}_z. \quad (2.5)$$

Note that rotation of the quadrotor is defined about its center of mass. Thus, torques are created from the quadrotor motion, the thrust forces, and the rotors spinning. Including these torques and rearranging gives the general form for the rotational equations of motion

$$I\dot{\omega} = -\omega \times I\omega + \sum_{k=1}^4 r_{k/cm} \times T_k + \omega \times I_r\Omega \quad (2.6)$$

where I is the inertia tensor of the quadrotor, I_r is the inertia tensor of the rotor, and $r_{k/cm}$ is the distance between the k th rotor and the center of mass of the quadrotor.

Quadrotors are generally designed to be symmetric about the three body axes. In

other words, their inertia tensors are diagonal matrices

$$I = \begin{bmatrix} I_x & 0 & 0 \\ 0 & I_y & 0 \\ 0 & 0 & I_z \end{bmatrix}. \quad (2.7)$$

Rotor inertia tensors exhibit the same property.

The rotational equations of motion are

$$I_x \dot{p} = -(I_z - I_y)qr + L(F_3 - F_4) \quad (2.8)$$

$$I_y \dot{q} = -(I_x - I_z)rp + L(F_2 - F_1) \quad (2.9)$$

$$I_z \dot{r} = -(I_y - I_x)pq + c_m \sum_{k=1}^4 F_k \quad (2.10)$$

where L is the distance from the rotor to the center of mass of the quadrotor (arm length) and c_m is a constant relating the thrust force and the yawing moment caused by spinning the rotors.

2.2 Aerodynamic Effects

The following section discusses the aerodynamic effects that are taken into account for the dynamics model presented in Section 2.3. The model includes the effects of aerodynamic drag, induced thrust due to translational flight, and rotor blade flapping. A free body diagram including these effects is shown in Figure 2-2. Note the differences from Figure 2-1, namely the inclusion of a sixth force (D) corresponding to aerodynamic drag and the four thrust forces are tilted and now have components in the \mathbf{b}_x and \mathbf{b}_y directions.

In aerodynamics, the velocity of the aircraft is often modeled as an apparent wind acting on the vehicle. The velocity of the vehicle in the body frame (\mathbf{v}) is related to the relative wind velocity vector (\mathbf{v}_{rel}) with the relationship

$$\mathbf{v}_{rel} = -\mathbf{v}. \quad (2.11)$$

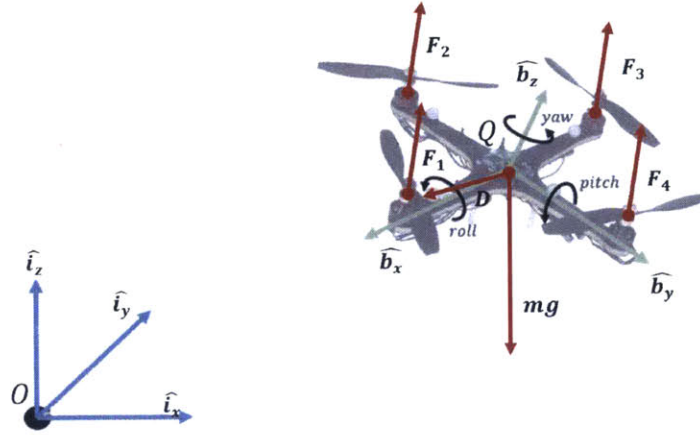


Figure 2-2: Free Body Diagram of a Quadrotor in Forward Flight with Body Reference Frame B Centered at Q and Inertial Reference Frame I Centered at O

The relative wind velocity vector acting on the k th rotor is defined as

$$\mathbf{v}_{rel,k} = u_k \mathbf{b}_x + v_k \mathbf{b}_y + w_k \mathbf{b}_z. \quad (2.12)$$

Similarly, the relative wind velocity vector acting on the center of mass is defined as

$$\mathbf{v}_{rel,cm} = u_{cm} \mathbf{b}_x + v_{cm} \mathbf{b}_y + w_{cm} \mathbf{b}_z. \quad (2.13)$$

2.2.1 Aerodynamic Drag

The aerodynamic drag is modeled as acting on the center of mass of the vehicle. Thus no moments are created by the drag force. The drag force is defined as

$$\mathbf{D} = \mathcal{C}_D \|\mathbf{v}_{rel,cm}\|^2 \hat{\mathbf{v}}_{rel,cm} \quad (2.14)$$

where \mathcal{C}_D is a drag constant that incorporates the effects of the coefficient of drag (C_D), density of air (ρ), and reference area (S),

$$\mathcal{C}_D = \frac{1}{2} \rho S C_D. \quad (2.15)$$

Calculating the aerodynamic drag in the body frame has the added benefit that the reference area is constant no matter the orientation of the vehicle. Quadrotors tend to be symmetric about all three body axes, thus the drag constant is the same when flying in either direction along a body axis. The drag constant along each body axes can be unique such that

$$\mathcal{C}_D = \begin{bmatrix} \mathcal{C}_{D,x} & 0 & 0 \\ 0 & \mathcal{C}_{D,y} & 0 \\ 0 & 0 & \mathcal{C}_{D,z} \end{bmatrix}. \quad (2.16)$$

2.2.2 Induced Thrust

Relative wind velocity changes the magnitude of thrust generated by a rotor through two main effects. The first is an increase in thrust due to horizontal translation (induced thrust). The other is a decrease in thrust if the relative wind in the b_z direction is negative. In short, the thrust from a rotor decreases in climb and increases in horizontal translation. To calculate the change in thrust due to these two effects

$$v_{i,k} = \frac{v_h^2}{\sqrt{u_k^2 + v_k^2 + (v_{i,k} + w_k)^2}} \quad (2.17)$$

$$T_k = \frac{F_k v_{i,k}}{v_{i,k} + w_k} \quad (2.18)$$

where v_h is the induced velocity in hover (determined using momentum theory [11]) and F_k is the commanded thrust (control input) [1]. Momentum theory states that for an actuator disk of area A with induced velocity v_h , and with air density ρ , the mass flow rate \dot{m} through the disk is

$$\dot{m} = \rho A v_h.$$

For a quadrotor in hover, the velocity far upstream of the actuator disk is zero and the velocity far downstream of the actuator disk is w_h . Conservation of momentum states that the total thrust T of the actuator disk is equal to the rate of change of

momentum

$$T = \dot{m}w_h.$$

Conservation of energy states

$$Tv_h = \frac{1}{2}\dot{m}w_h^2.$$

Substituting in and solving for v_h

$$v_h = \frac{1}{2}w_h.$$

Using this value for v_h and the equation for \dot{m}

$$T = \dot{m}w_h = 2\rho Av_h^2.$$

Finally, solving for v_h

$$v_h = \sqrt{\frac{T}{2A\rho}}. \quad (2.19)$$

Equation 2.17 results in a fourth order polynomial when solving for the induced velocity. In climb ($w_k < 0$), the equation has only one positive real root which corresponds to the physical solution [10]. In hover ($w_k = 0$) the induced velocity is v_h . In descent ($w_k > 0$), the airflow through the rotor is steady, therefore the momentum theory based solution listed above is not valid.

The main limitation of the model presented in equations 2.17 & 2.18 is that it only holds when $w_k \geq 0$ or $w_k > 2|v_k|$ [10]. When w_k is not in this range, the rotor is in Vortex Ring State, a region where the aerodynamics are unsteady and momentum theory breaks down. Generally, the solution is to fly quickly through this flight regime to avoid the dynamic instabilities that occur.

2.2.3 Blade Flapping

Figure 2-2 pictures the thrust vectors tilted away from the \mathbf{b}_z axis. This is due to rotor blade flapping. This effect occurs due to a difference in lift experienced on the advancing and retreating sides of the rotor while in translational flight. Specifically,

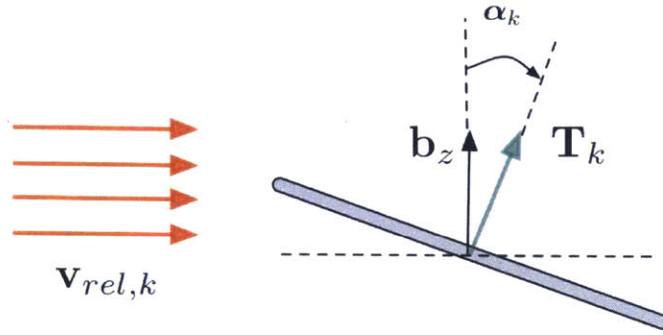


Figure 2-3: Blade Flap Angle of the Rotor Due to a Relative Wind [1]

due to the translational velocity of the vehicle, the advancing rotor blade observes a higher relative velocity than the retreating blade, and therefore produces more lift. This results in an aerodynamic load differential across the rotor, causing the blades to flap during rotation. The loading cycles of the rotor occur at the same frequency as its rotation. This causes a resonance that causes the maximum deflection of the blade to occur 90 degrees out of phase [12]. This results in the entire rotor disc tilting away from the apparent wind, deflecting the thrust force away from the \mathbf{b}_z axis.

Blade flapping is a function of the relative velocity in the x-y direction in the body frame. In sustained forward flight, the relative wind over each rotor is assumed to be equal. As such, the blade flap angle α_k (see Figure 2.2.3 can be approximated as

$$\alpha = k_f \sqrt{u_{cm}^2 + v_{cm}^2} \quad (2.20)$$

where k_f is a constant representing the relative displacement of a particular rotor [1]. The value of k_f is the same for all four rotors (as they are assumed to be the same type of rotor). The actual value parameter k_f must be determined experimentally, but can estimated given that blade flap angle tends to be on the order of one degree in moderate wind [10].

The primary effect of blade flapping is the tilting of the thrust vector off of the

\mathbf{b}_z axis. Using geometry, the thrust vector of the k th rotor (\mathbf{T}_k) is

$$\mathbf{T}_k = T_k(\bar{u}_k \sin \alpha \mathbf{b}_x + \bar{v}_k \sin \alpha \mathbf{b}_y + \cos \alpha) \quad (2.21)$$

where \bar{u}_k and \bar{v}_k are the x and y components of the relative wind vector of the k th rotor normalized in the x-y body plane

$$\bar{x}_k = \frac{u_k}{\sqrt{u_k^2 + v_k^2}} \quad (2.22)$$

$$\bar{v}_k = \frac{v_k}{\sqrt{u_k^2 + v_k^2}} \quad (2.23)$$

2.3 Equations of Motion

In this section, the equations of motion from Section 2.1 are augmented with the aerodynamic effects described in Section 2.2. The resulting equations of motion describe the dynamics model used to simulate a quadrotor in forward flight.

From Equation 2.3, the general form for the translational dynamics is

$$m \begin{bmatrix} \ddot{x} \\ \ddot{y} \\ \ddot{z} \end{bmatrix} = {}^I R^B \begin{bmatrix} C_1 \\ C_2 \\ C_3 \end{bmatrix}_B - \begin{bmatrix} 0 \\ 0 \\ mg \end{bmatrix}_I \quad (2.24)$$

Note that the thrust forces now have components in the \mathbf{b}_x and \mathbf{b}_y axes due to blade flapping. The equation for C_1 , C_2 , and C_3 are

$$C_1 = \left(\mathcal{C}_{D,x} \|\mathbf{v}_{rel,cm}\| u_{cm} + \sum_{k=1}^4 \bar{u}_k \sin \alpha T_{i,k} \right) \quad (2.25)$$

$$C_2 = \left(\mathcal{C}_{D,y} \|\mathbf{v}_{rel,cm}\| v_{cm} + \sum_{k=1}^4 \bar{v}_k \sin \alpha T_{i,k} \right) \quad (2.26)$$

$$C_3 = \left(\mathcal{C}_{D,z} \|\mathbf{v}_{rel,cm}\| w_{cm} + \sum_{k=1}^4 \cos \alpha T_{i,k} \right) \quad (2.27)$$

and the rotation matrix between the inertial and body frames (Equation 2.1) is

$${}^I R^B = \begin{bmatrix} c\theta c\psi & s\phi s\theta c\psi - c\phi s\psi & c\phi s\theta c\psi + s\phi s\psi \\ c\theta s\psi & s\phi s\theta s\psi + c\phi c\psi & c\phi s\theta s\psi + s\phi c\psi \\ -s\theta & s\phi c\theta & c\phi c\theta \end{bmatrix}. \quad (2.28)$$

From Equation 2.6, the general form of the rotational dynamics is

$$I\dot{\omega} = -\omega \times I\omega + \sum_{k=1}^4 r_{k/cm} \times T_k + \omega \times I_r \Omega. \quad (2.29)$$

Augmenting the hover equation with the aerodynamic effects results in the following rotational equations of motion

$$I_x \dot{p} = -(I_z - I_y)qr - \sum_{i=1}^4 d\bar{v}_k \sin \alpha(T_k) + L \cos \alpha(T_4 - T_2) \quad (2.30)$$

$$I_y \dot{q} = -(I_x - I_z)rp - \sum_{i=1}^4 d\bar{u}_k \sin \alpha(T_k) + L \cos \alpha(T_3 - T_1) \quad (2.31)$$

$$I_z \dot{r} = -(I_y - I_x)pq - L \sin \alpha(\bar{v}_1 T_1 - \bar{v}_3 T_3 + \bar{u}_4 T_4 - \bar{u}_2 T_2) + c_m \sum_{i=1}^4 F_k. \quad (2.32)$$

To simulate the system, the rotational kinematics for a 3-2-1 Euler angle sequence are used

$$\dot{\phi} = p + q \sin \phi \tan \theta + r \cos \phi \tan \theta \quad (2.33)$$

$$\dot{\theta} = q \cos \phi - r \sin \phi \quad (2.34)$$

$$\dot{\psi} = q \sin \phi \sec \theta + r \cos \phi \sec \theta. \quad (2.35)$$

Chapter 3

System Architecture and Control

This chapter describes the system architecture and control algorithms used for the quadrotor in forward flight. The outer loop control algorithms described in this chapter are similar to those presented in [13]. The attitude control law presented does not assume near hover flight regimes, making it a good fit for the application of sustained forward flight.

First the overall system architecture is described followed by a discussion of the control algorithms employed to control a quadrotor flying at high speed. The full system was implemented using Simulink [14]. Graphical implementations of the control laws and equations of motion are provided throughout this chapter in the form of Simulink diagrams. Simulation results including equilibrium states and operating limits are discussed at the end of the chapter.

3.1 System Architecture

The system architecture is designed using two levels of successive loop closure. The outer most loop is position control loop. This loop takes as inputs a set of reference position and velocity along with measured position and velocity. It outputs a desired attitude, desired angular rate, and motor throttle command to be passed to the next level in. The inner control loop is an attitude controller. This loop takes as inputs the output of the position controller (desired attitude, angular rate, throttle command)

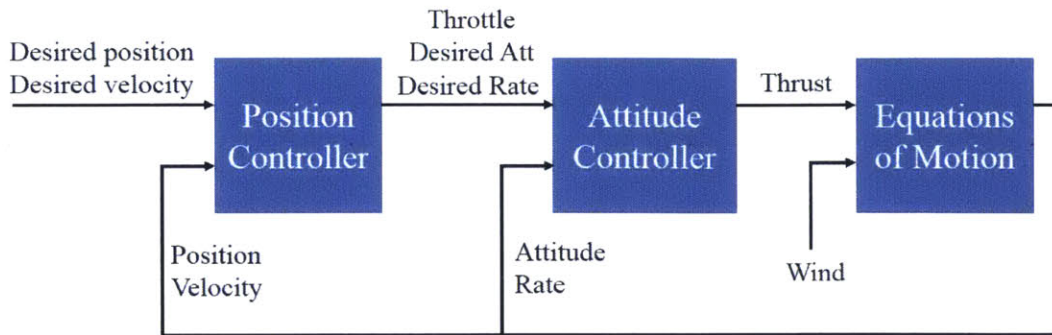


Figure 3-1: Top Level Block Diagram of the Simulated System

along with measured values for the attitude and angular rate of the quadrotor. Motor commands, which are the outputs of this control loop, which are fed into the equations of motion described in Chapter 2 if simulating the system, or to actual motors if using hardware. The system dynamics take motor commands and wind speed as inputs and output the measured values for position, velocity, attitude, and angular rate to be fed back to the inner and outer control loops. Note that the implementation of the system presented in this chapter uses wind speed as a direct input into the system dynamics. This method was chosen because it most accurately matches the experimental set up using the wind tunnel to be presented in Chapter 4. Another Simulink diagram was implemented using a velocity controller as the outer control loop, commanding non-zero reference velocities, and eliminating wind speed as an input into the system dynamics. The resulting behavior was identical to the presented system architecture, confirming that using a wind tunnel as a proxy for high speed flight does not change the dynamic response. A top level block diagram of the system is shown in Figure 3-1 including inputs and outputs of each block. Figure 3-2 is the top level view of the Simulink model implementation of a quadrotor in sustained forward flight.

3.2 Feedback Control

This section describes the control algorithms used to stabilize a quadrotor in forward flight. The outer loop controller will first be described, followed by the inner loop

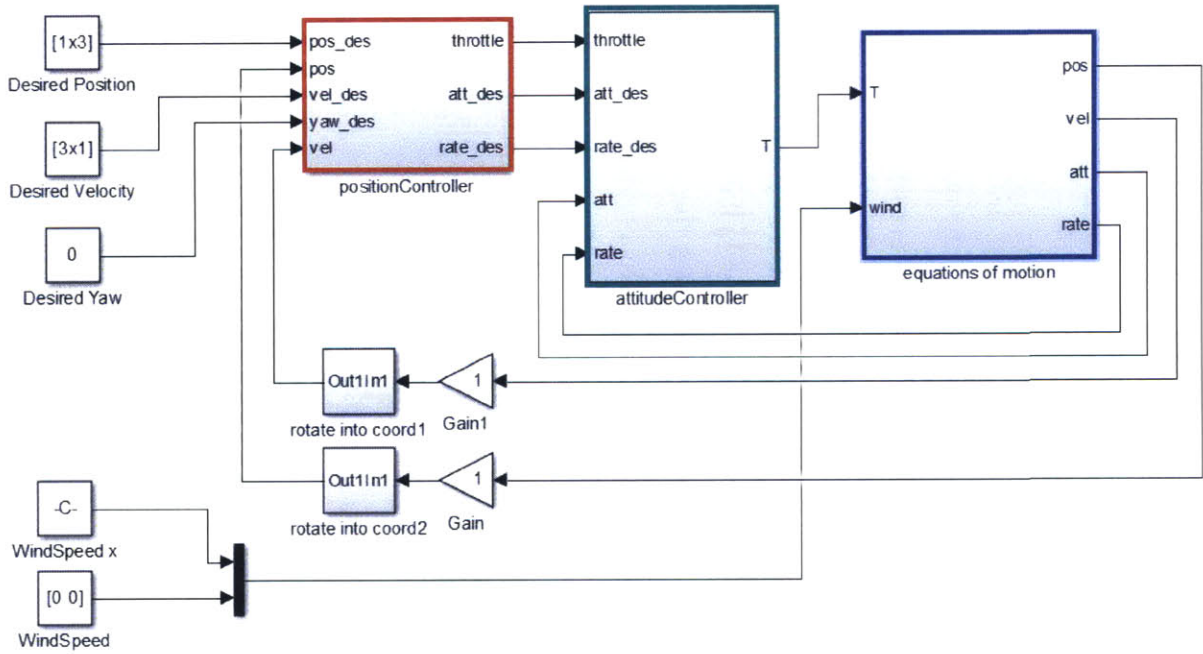


Figure 3-2: Top Level Simulink Diagram of Simulated System

controller. Simulink implementations of both control loops are also provided. The system is controlled using two successive control loops which match the controller of the physical system described in Section 5.2. All positions, velocities, and attitudes used in the control loops are in the inertial frame I .

3.2.1 Position Control

The position control loop (also referred to as the outer control loop) takes as inputs the reference position and velocity and the measured position and velocity. The measured values are fed into the outer control loop from the system dynamics. The reference values are inputs into the system as a whole and can be set directly or through a trajectory generator. The position control loop is a two step process. First, desired accelerations are computed using the position and velocity inputs. The desired accelerations are then used to compute a motor throttle command and desired attitude and angular rate for the quadrotor.

To compute the desired acceleration vector, a position error vector (\mathbf{e}_{pos}) and a velocity error vector (\mathbf{e}_{rate}) are calculated

$$\mathbf{e}_{pos} = \begin{bmatrix} x_{des} & y_{des} & z_{des} \end{bmatrix}^T - \begin{bmatrix} x_{meas} & y_{meas} & z_{meas} \end{bmatrix}^T \quad (3.1)$$

$$\mathbf{e}_{rate} = \begin{bmatrix} \dot{x}_{des} & \dot{y}_{des} & \dot{z}_{des} \end{bmatrix}^T - \begin{bmatrix} \dot{x}_{meas} & \dot{y}_{meas} & \dot{z}_{meas} \end{bmatrix}^T \quad (3.2)$$

where $\begin{bmatrix} x_{des} & y_{des} & z_{des} \end{bmatrix}^T$ is the desired position vector, $\begin{bmatrix} x_{meas} & y_{meas} & z_{meas} \end{bmatrix}^T$ is the measured position vector, $\begin{bmatrix} \dot{x}_{des} & \dot{y}_{des} & \dot{z}_{des} \end{bmatrix}^T$ is the desired velocity vector, and $\begin{bmatrix} \dot{x}_{meas} & \dot{y}_{meas} & \dot{z}_{meas} \end{bmatrix}^T$ is the measured velocity vector. The errors are mapped into acceleration commands using a PID controller

$$\begin{bmatrix} \ddot{x}_{cmd} & \ddot{y}_{cmd} & \ddot{z}_{cmd} \end{bmatrix}^T = K_{P,pos} \mathbf{e}_{pos} + K_{I,pos} \int_0^t \mathbf{e}_{pos} + K_{D,pos} \mathbf{e}_{vel} \quad (3.3)$$

where $K_{P,pos}$, $K_{I,pos}$, and $K_{D,pos}$ are 3x3 diagonal, positive definite gain matrices.

Gravity is then taken into account to compute the desired accelerations

$$\begin{bmatrix} \ddot{x}_{des} & \ddot{y}_{des} & \ddot{z}_{des} \end{bmatrix}^T = \begin{bmatrix} \ddot{x}_{cmd} & \ddot{y}_{cmd} & \ddot{z}_{cmd} \end{bmatrix}^T + \begin{bmatrix} 0 & 0 & g \end{bmatrix}. \quad (3.4)$$

To compute the motor throttle command (h_{cmd}), the desired accelerations are turned into forces, summed, and mapped to a throttle command

$$h_{cmd} = \frac{1}{k_{motor}} m(\ddot{x}_{des} + \ddot{y}_{des} + \ddot{z}_{des}) \quad (3.5)$$

using an experimentally-determined motor constant (k_{motor}). The motor throttle command is then output to the inner control loop.

The second step of the outer control loop computes the desired attitude and angular rate given the desired accelerations. For this step, the attitude of the vehicle in the inertial frame is described by quaternion \mathbf{q} and the angular rates in the body frame B defined as Ω_b . The quaternion \mathbf{q} is defined as

$$\mathbf{q} = \begin{bmatrix} q^0 \\ \vec{q} \end{bmatrix}$$

where q^0 is the scalar component and \vec{q} is the vector component. The desired force vector in the inertial frame is defined as

$$\mathbf{F}_{i,des} = m(\ddot{x}_{des}\mathbf{i}_x + \ddot{y}_{des}\mathbf{i}_y + \ddot{z}_{des}\mathbf{i}_z) \quad (3.6)$$

and $\mathbf{F}_{b,des}$ is the desired force vector in the body frame. Equation 3.11 in [13] gives a relation between the desired attitude quaternion (\mathbf{q}_{des}) and the desired force vector

$$\begin{bmatrix} 0 \\ \bar{\mathbf{F}}_{i,des} \end{bmatrix} = \mathbf{q}_{des}^* \otimes \begin{bmatrix} 0 \\ \bar{\mathbf{F}}_{b,des} \end{bmatrix} \otimes \mathbf{q}_{des} \quad (3.7)$$

where $\bar{\mathbf{F}}_{b,des}$ and $\bar{\mathbf{F}}_{i,des}$ are unit vectors,

$$\bar{\mathbf{F}}_{b,des} = \frac{\mathbf{F}_{b,des}}{\|\mathbf{F}_{b,des}\|} = \begin{bmatrix} 0 & 0 & 1 \end{bmatrix}^T \quad (3.8)$$

$$\bar{\mathbf{F}}_{i,des} = \frac{\mathbf{F}_{i,des}}{\|\mathbf{F}_{i,des}\|}. \quad (3.9)$$

\mathbf{q}_{des}^* is the quaternion conjugate of \mathbf{q}_{des} , and \otimes is the quaternion multiplication operator. In this formulation, \mathbf{q}_{des} corresponds to the quadrotor attitude (not including desired yaw) that aligns the body frame force vector with the inertial force vector. The minimum-angle quaternion rotation between the two force vectors in \mathbb{R}^3 is [15]

$$\mathbf{q}_{des} = \frac{1}{\sqrt{2(1 + \bar{\mathbf{F}}_{i,des}^T \bar{\mathbf{F}}_{b,des})}} \begin{bmatrix} 1 + \bar{\mathbf{F}}_{i,des}^T \bar{\mathbf{F}}_{b,des} \\ \bar{\mathbf{F}}_{i,des}^T \times \bar{\mathbf{F}}_{b,des} \end{bmatrix}. \quad (3.10)$$

Note that Equation 3.10 does not produce a unique desired attitude quaternion. In particular, quaternions define the special orthogonal group $S0(3)$ in two ways. This results in \mathbf{q} and $-\mathbf{q}$ defining the same attitude [13]. To remove this ambiguity, the sign of \mathbf{q}_{des} is chosen to match the sign of \mathbf{q}_{des} at the previous time step.

The desired attitude quaternion is then rotated by the desired yaw angle (ψ_{des}) to compute the full desired vehicle attitude quaternion

$$\mathbf{q}_{des,f} = \mathbf{q}_{des} \otimes \begin{bmatrix} \cos(\psi_{des}/2) & 0 & 0 & \sin(\psi_{des}/2) \end{bmatrix}^T. \quad (3.11)$$

In the Simulink implementation of the system, the desired attitude quaternion is converted into Euler angles and output to the inner control loop.

The desired angular rate ($\Omega_{b,des}$) is calculated by taking the time derivative of $\bar{\mathbf{F}}_{i,des}$. From [13], the angular rates in the x and y body axes is

$$(\Omega_{b,des})_{xy} = \bar{\mathbf{F}}_{i,des} \times \dot{\bar{\mathbf{F}}}_{i,des} \quad (3.12)$$

where the time derivative of the inertial desired force vector is

$$\dot{\mathbf{F}}_{i,des} = \frac{\dot{\mathbf{F}}_{i,des}}{\|\mathbf{F}_{i,des}\|} - \frac{\mathbf{F}_{i,des}(\mathbf{F}_{i,des}^T \dot{\mathbf{F}}_{i,des})}{\|\mathbf{F}_{i,des}\|^3}. \quad (3.13)$$

The z component of the angular velocity (yaw rate), is directly computed from the input yaw command

$$(\Omega_{b,des})_z = \dot{\psi}_{des}. \quad (3.14)$$

The desired angular rate of the quadrotor is then output to the inner control loop. Figure 3-3 is the Simulink model for the position control loop. The figure includes a complete view of the outer control loop along with a detailed view on the first step, calculating a desired force vector from position and velocity (orange block), and the second step, calculating desired attitude, angular rate, and throttle command from the desired force vector (yellow block).

3.2.2 Attitude Control

The attitude control loop (also referred to as the inner control loop) takes as inputs desired attitude and angular rates from the outer control loop and measured attitude and angular rates from the system dynamics. Its purpose is to output motor commands to the system dynamics. First, an attitude error vector (\mathbf{e}_{att}) and an angular rate error vector (\mathbf{e}_{rate}) are calculated

$$\mathbf{e}_{att} = \begin{bmatrix} \phi_{des} & \theta_{des} & \psi_{des} \end{bmatrix}^T - \begin{bmatrix} \phi_{meas} & \theta_{meas} & \psi_{meas} \end{bmatrix}^T \quad (3.15)$$

$$\mathbf{e}_{rate} = \begin{bmatrix} p_{des} & q_{des} & r_{des} \end{bmatrix}^T - \begin{bmatrix} p_{meas} & q_{meas} & r_{meas} \end{bmatrix}^T \quad (3.16)$$

where $\begin{bmatrix} \phi_{des} & \theta_{des} & \psi_{des} \end{bmatrix}^T$ is the desired attitude vector, $\begin{bmatrix} \phi_{meas} & \theta_{meas} & \psi_{meas} \end{bmatrix}^T$ is the measured attitude vector, $\begin{bmatrix} p_{des} & q_{des} & r_{des} \end{bmatrix}^T$ is the desired angular rate vector, and $\begin{bmatrix} p_{meas} & q_{meas} & r_{meas} \end{bmatrix}^T$ is the measured angular rate. The errors are mapped into roll,

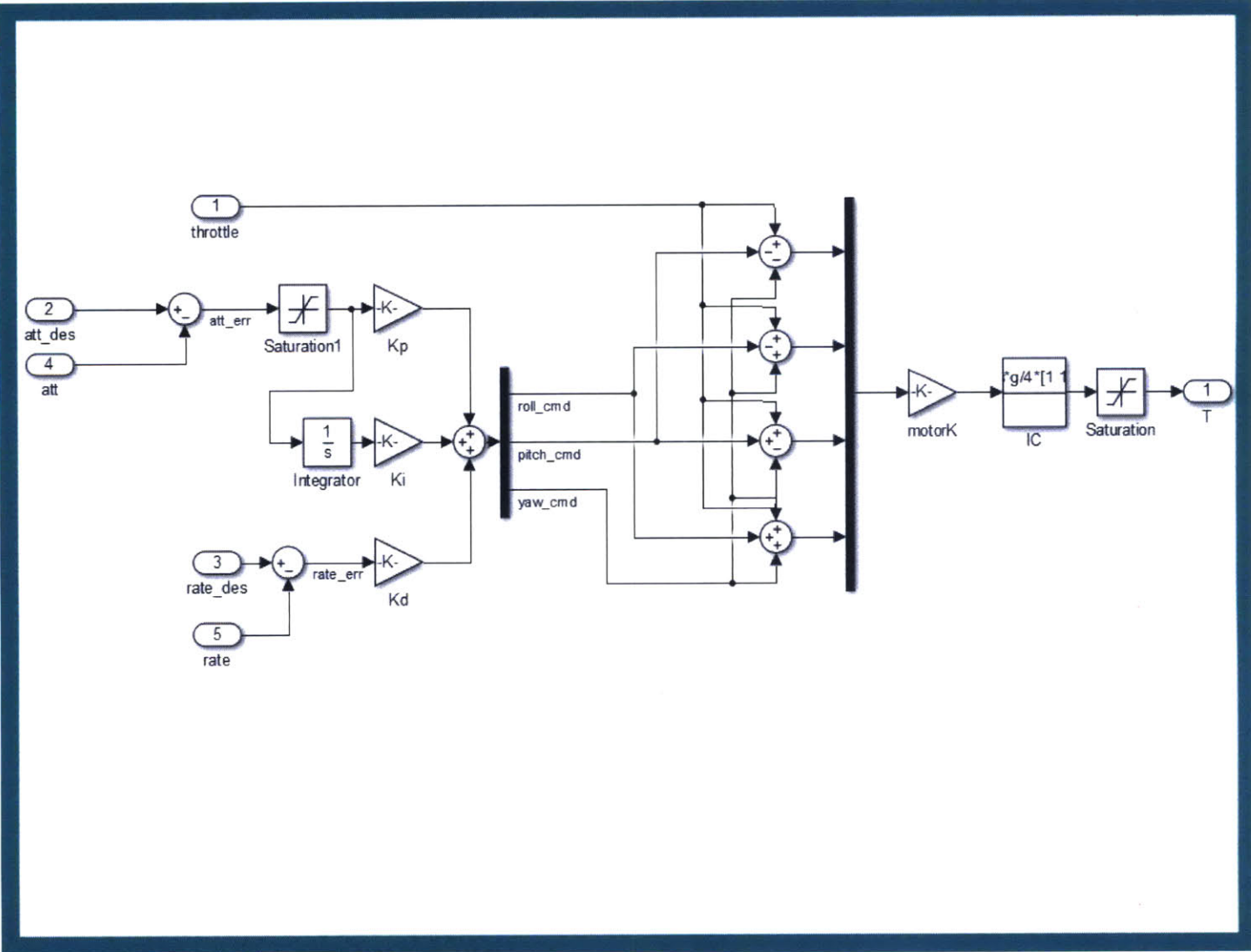


Figure 3-4: Simulink Diagram of Block "attitudeController". This Block Corresponds to the Attitude Control Loop (Inner Control Loop Described in Section 3.2.2

pitch, and yaw commands (ϕ_{cmd} , θ_{cmd} , and ψ_{cmd} , respectively) using a PID controller

$$\begin{bmatrix} \phi_{cmd} & \theta_{cmd} & \psi_{cmd} \end{bmatrix}^T = K_{P,att} \mathbf{e}_{att} + K_{I,att} \int_0^t \mathbf{e}_{att} + K_{D,att} \mathbf{e}_{rate} \quad (3.17)$$

where $K_{P,att}$, $K_{I,att}$, and $K_{D,att}$ are 3x3 diagonal, positive semi-definite gain matrices. The angle commands are then used with the motor throttle input (h_{cmd}) to calculate motor commands

$$\begin{bmatrix} m_1 \\ m_2 \\ m_3 \\ m_4 \end{bmatrix} = \begin{bmatrix} 1 & 0 & -1 & -1 \\ 1 & -1 & 0 & 1 \\ 1 & 0 & 1 & -1 \\ 1 & 1 & 0 & 1 \end{bmatrix} \begin{bmatrix} h_{cmd} \\ \phi_{cmd} \\ \theta_{cmd} \\ \psi_{cmd} \end{bmatrix}. \quad (3.18)$$

In simulation, the motor commands are then converted to motor thrusts (F_1 , F_2 , F_3 , F_4) in Newtons using an experimentally-determined motor constant (k_{motor}) and then saturated to within the actuator limits

$$F_k = k_{motor} m_k. \quad (3.19)$$

The thrust forces are then fed into the system dynamics as the outputs of this control loop. Figure 3-4 is the Simulink model for the attitude control loop.

3.3 System Dynamics

The system dynamics are the quadrotor's response given external forces and moments on the vehicle. This block takes motor commands as inputs. Note that in the simulation, wind speed is also an input so that the system dynamics better match the wind tunnel experimental setup, which will be described in Chapter 4. The system dynamics output actual (or measured) values for the attitude, angular rate, position, and velocity of the quadrotor. Experimentally, this block is the physical vehicle. In simulation, it is an implementation of the equations of motion presented in Chapter 2.

Figure 3-5 is the Simulink model for the dynamics of the system as defined in

Chapter 2, including both aerodynamic effects and rigid body dynamics. Figure 3-6 shows the implementation of the stock six degree-of-freedom block which propagates the simulated system forward in time given forces and moments on the body as inputs.

3.4 Simulation Results

This section discusses the results obtained from the Simulink implementation of the system described throughout this chapter. The main topics discussed include the steady state attitude response of the vehicle at different operating speeds, forward flight effects on the actuation limits of the vehicle, and the overall performance of the system with the controller presented in Section 3.2.

Values used for the physical parameters and aerodynamic properties of the system for the simulation match the physical parameters and aerodynamic properties of the actual vehicle used in flight experiments to be described in Chapter 6. The methods of obtaining these values are discussed in Chapter 5.

The primary purpose of the simulation is to provide insight into the long term dynamics and limitations of the system described in this chapter. This insight is used to inform the experimental design of the flight tests to be described in Chapter 6. The simulation results will also be compared to experimental results to show the validity of the model presented in Chapter 2.

The simulation starts with zero initial conditions for all states of the quadrotor. The motor thrusts are initialized with forces needed to maintain hover

$$F_{k,0} = \frac{mg}{4}. \quad (3.20)$$

The simulation commands the following reference inputs

$$\begin{bmatrix} x_{des} & y_{des} & z_{des} \end{bmatrix}^T = \begin{bmatrix} 0.1 \text{ m} & 0 & 0 \end{bmatrix}^T \quad (3.21)$$

$$\begin{bmatrix} \dot{x}_{des} & \dot{y}_{des} & \dot{z}_{des} \end{bmatrix}^T = \begin{bmatrix} 0 & 0 & 0 \end{bmatrix}^T \quad (3.22)$$

$$\psi_{des} = 0 \quad (3.23)$$

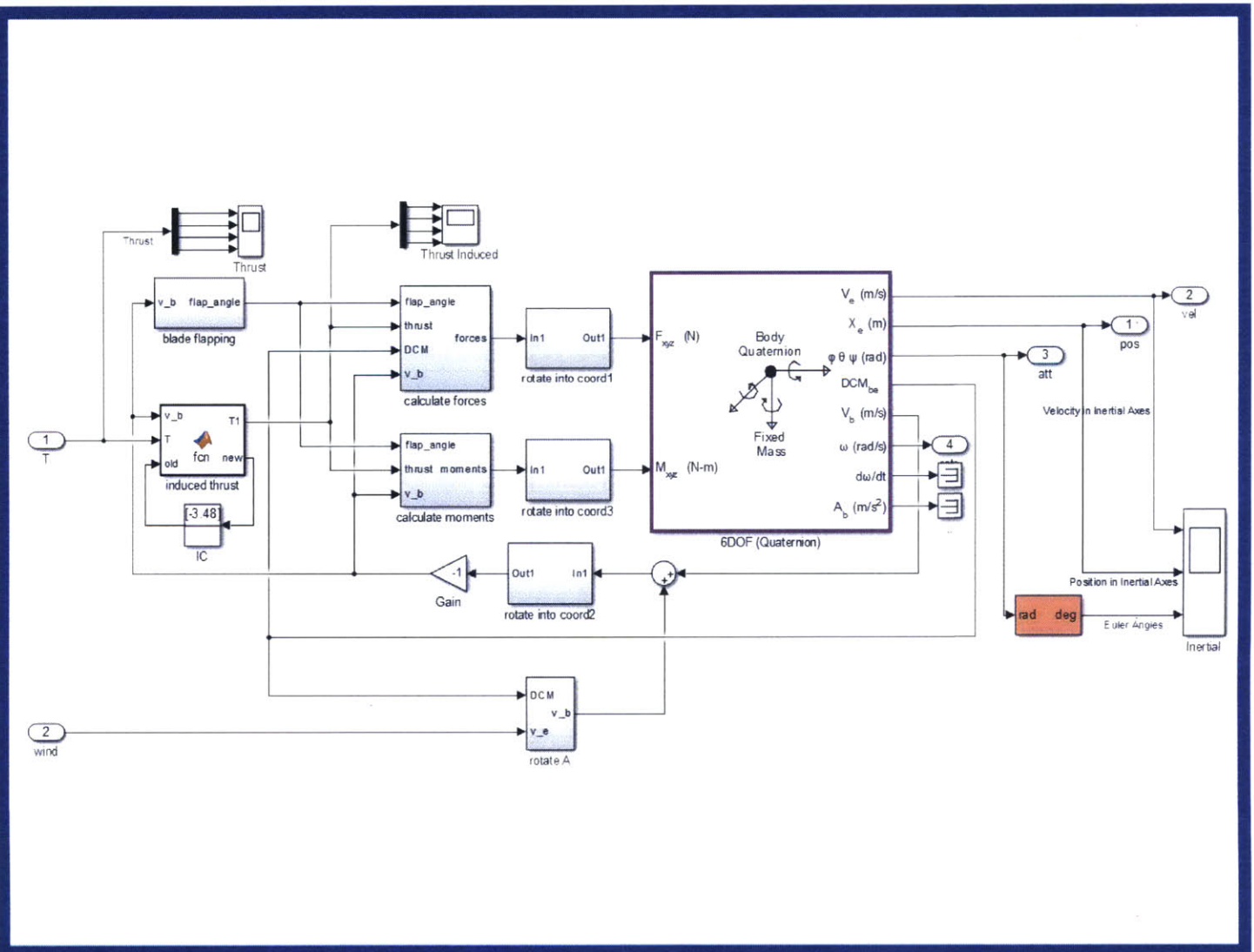
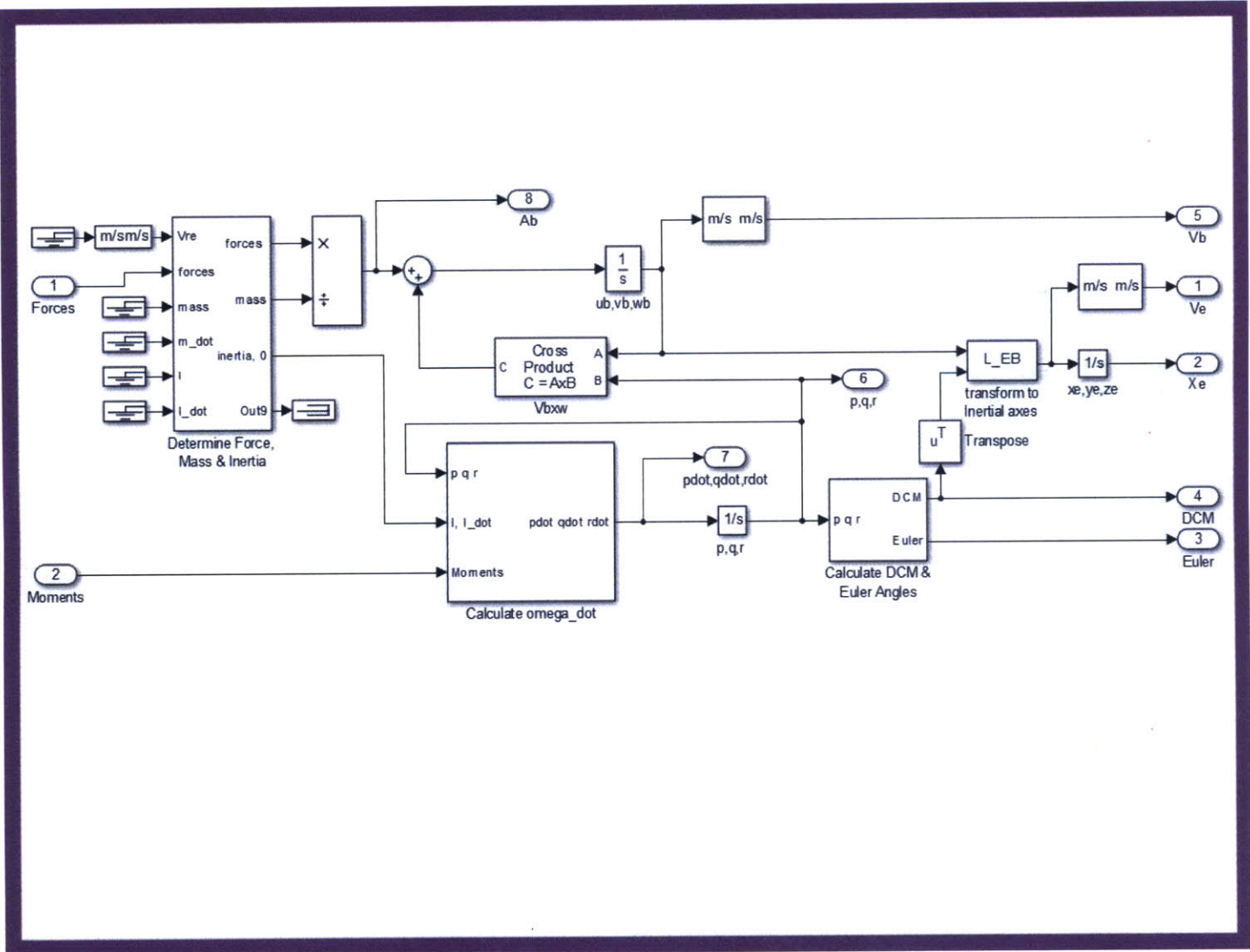


Figure 3-5: Simulink Diagram of Block "equations of motion" Corresponds to the System Dynamics Described in Section 3.3

Figure 3-6: Simulink Diagram of Block "equations of motion/6DOF (Quaternion)"



and a constant wind speed is added as a direct input into the system dynamics.

3.4.1 Steady State Attitude Response

Unlike at hover conditions, the steady state attitude of a quadrotor in forward flight is nonzero. This is due to the coupling of attitude and velocity that governs quadrotor motion. In this section, the results are generated using a constant wind speed in the negative x direction in the inertial frame. The quadrotor being simulated is equally symmetric about both the x and y body axes. In other words,

$$I_x = I_y.$$

Thus, the response of the system would be of the same magnitude and form whether the wind speed was applied along the x or the y inertial axes. Wind speed along the x inertial axis corresponds to a response in pitch while wind speed along the y inertial axis corresponds to roll.

Figure 3-7 shows the steady state value for the quadrotor pitch at wind speeds ranging from 0 to 11 m/s (0 to 25 mph). The figure shows a nonlinear relationship between the steady state pitch and wind speed, a quadratic relationship to be specific

$$\theta_{ss} \propto u_{cm,rel}^2. \quad (3.24)$$

Similarly,

$$\phi_{ss} \propto v_{cm,rel}^2. \quad (3.25)$$

3.4.2 Actuation Limits

Determining the limits of a system is important for informing experimental design for testing the physical quadrotor. Similar operating limits between the simulated and physical system would be evidence to suggest that the model is valid. As in Section 3.4.1, results are generated using a wind in the negative x direction in the inertial

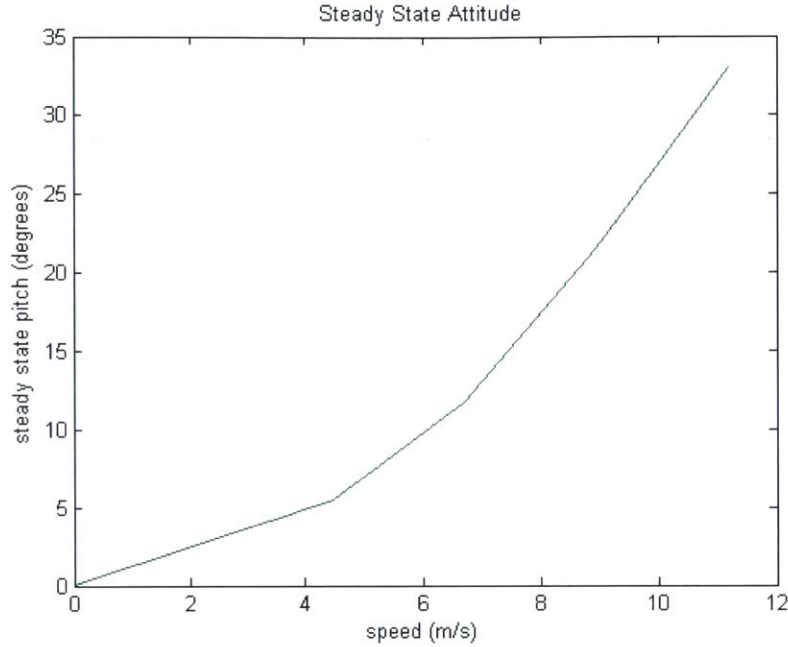


Figure 3-7: Steady State Pitch of the Simulated System as a Function of Wind Speed

frame due to the symmetry of the quadrotor.

For the simulated system, the fastest wind speed in which the quadrotor could return to the commanded position within a reasonable time is 13.5 m/s (30 mph). The quadrotor could make progress towards the commanded position at 14 m/s (31 mph) but displayed an prohibitively long return time (>100 seconds). Figure 3-8 shows the simulated states of the system while in a 14.5 m/s (32 mph) wind along with the calculated induced thrust forces (T_1, T_2, T_3, T_4). Note that the position in the x direction of the inertial frame drifts and never turns to return back to the commanded position. The motor thrusts hit their upper limits at 13 seconds and saturate for the rest of the simulation.

Figure 3-9 shows the simulated system response at the maximum controllable speed, 13.5 m/s (30 mph). Similar to Figure 3-8, the induce thrust forces hit their upper limits, this time around 16 seconds in. However, the position in the x direction of the inertial frame is able to return to the reference position and the induced thrust drops below the upper saturation point. Note that the steady state pitch command

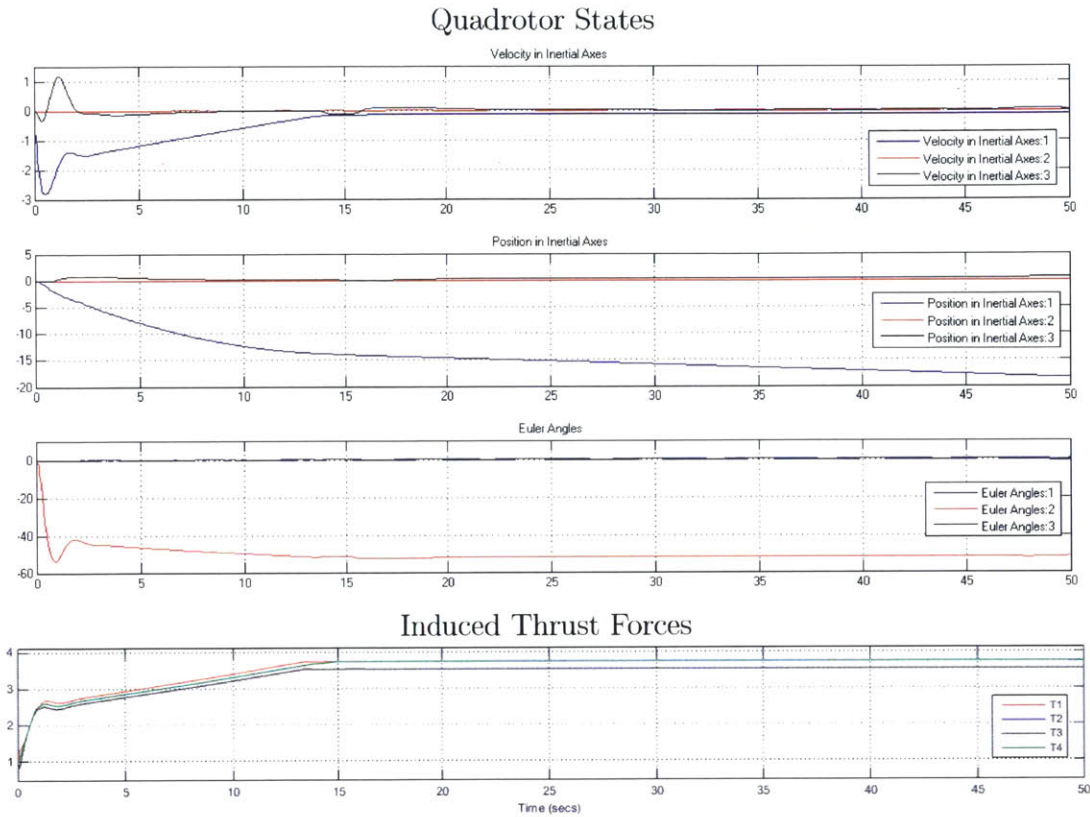


Figure 3-8: System Response of Simulated Quadrotor Above Maximum Operating Speed (32 mph). From Top to Bottom, The Plots Show Velocity in the Inertial Frame, Position in the Inertial Frame, Attitude in Euler Angles, and the Induced Thrust Forces All With Respect To Time.

at maximum speed is roughly 45° .

3.4.3 Control Performance

Response time of the system is largely governed by the controller parameters. The control gains were chosen to promote stability and controllability over low rise times. This section discusses the step response of the system when a wind force is instantaneously applied to it. The ability of the quadrotor to track reference commands is also discussed.

In the simulation, a wind force is applied to a quadrotor initialized at hover instantaneously at $t = 0$. The quadrotor then attempts to return to a constant

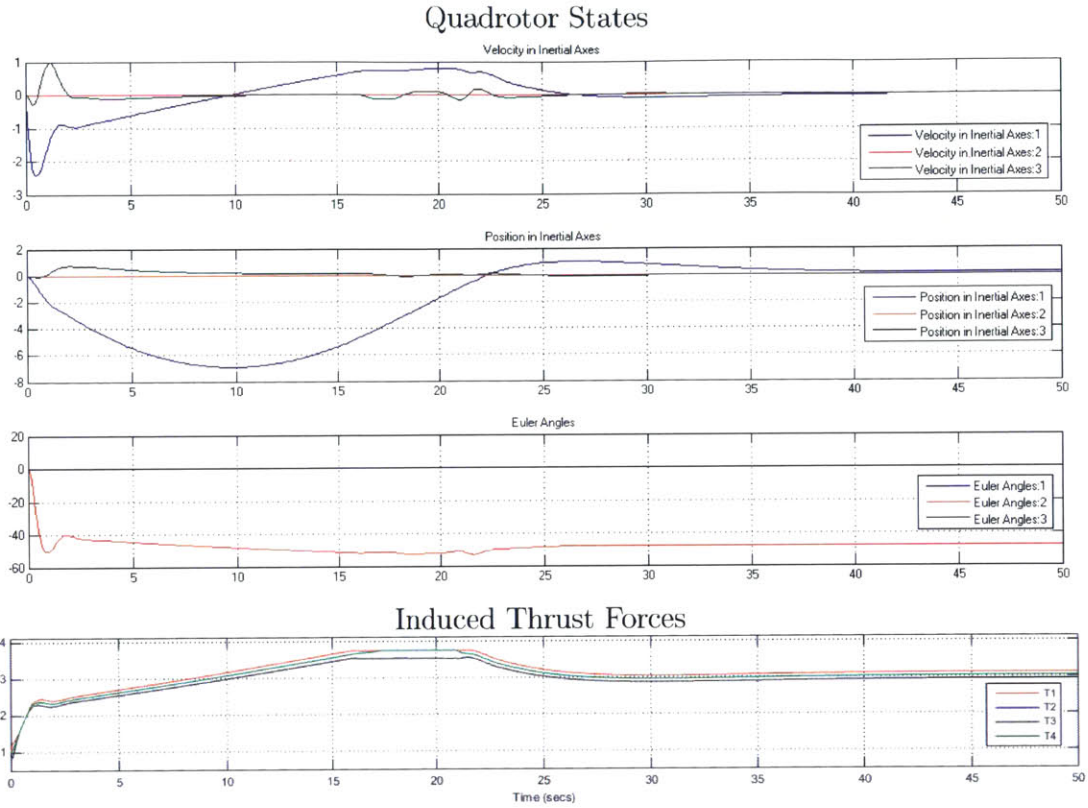


Figure 3-9: System Response of Simulated Quadrotor at Maximum Operating Speed (30 mph) From Top to Bottom, The Plots Show Velocity in the Inertial Frame, Position in the Inertial Frame, Attitude in Euler Angles, and the Induced Thrust Forces All With Respect To Time.

reference position. To quantify the response time of the system, the rise time (t_r) is defined as the earliest time at which the quadrotor is within .01 m of the reference position. The settling time (t_s) is defined as the earliest time at which the quadrotor is within .005 m of the reference position and remains within $\pm .005$ m from the reference position. Table 3.1 provides the values of t_r and t_s at speeds from 0 m/s to 13.5 m/s (0 to 30 mph).

The entry in Table 3.1 for a wind speed of 13.5 m/s corresponds to the graphs in Figure 3-9. Note that it has a significantly shorter rise time and later settling time than the next slower speed. This is due to the overshoot (seen in Figure 3-9) in the x position at this wind speed. Slower wind speeds do not result in a similar overshoot

Table 3.1: Rise and Settling Time of the Simulated System at High Speed

Wind Speed (m/s)	Rise Time, t_r (s)	Settling Time, t_s (s)
0	1	2
2.2	12	17
4.8	20	25
6.7	24	30
9	29	33
11.2	31	35
13.5	23	47

and rather smoothly approach the reference position. Figure 3-10 is a graph of r_t and r_s as a function of wind speed, up to 11.2 m/s (25 mph). This shows a nonlinear relationship between rise time/settling time and wind speed. Specifically

$$t_r \propto u_{cm,rel}^{\frac{1}{2}} \quad (3.26)$$

$$t_s \propto u_{cm,rel}^{\frac{1}{2}} \quad (3.27)$$

To test the ability of the system to track non-constant reference inputs, a sine wave of amplitude 0.5 m and frequency 1 rad/s

$$x_{ref}^* = x_{ref} + 0.5 \sin t \quad (3.28)$$

was added to the initial reference x position. Figure 3-11 shows the the system response while tracking x_{ref}^* with a wind speed of 9 m/s (20 mph). After the expected rise time (Table 3.1), the quadrotor accurately tracks the sine wave. This demonstrates that the quadrotor maintains an adequate amount of control authority while counteracting a wind speed of 9 m/s (20 mph). Similar results are observed up to 12 m/s (27 mph). At higher speeds, the upper limit of the induced thrust forces prevent accurate reference tracking in one direction.

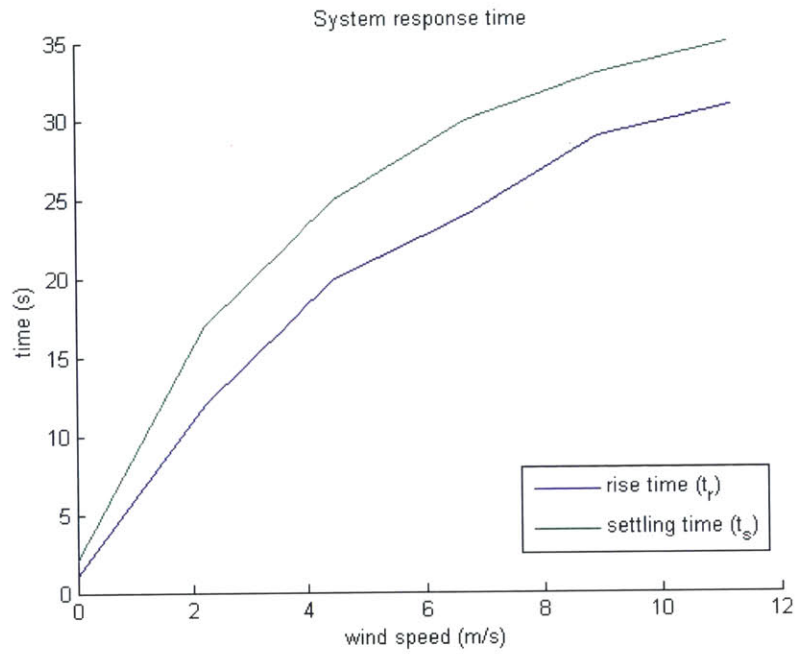


Figure 3-10: System Response Time as a Function of Wind Speed

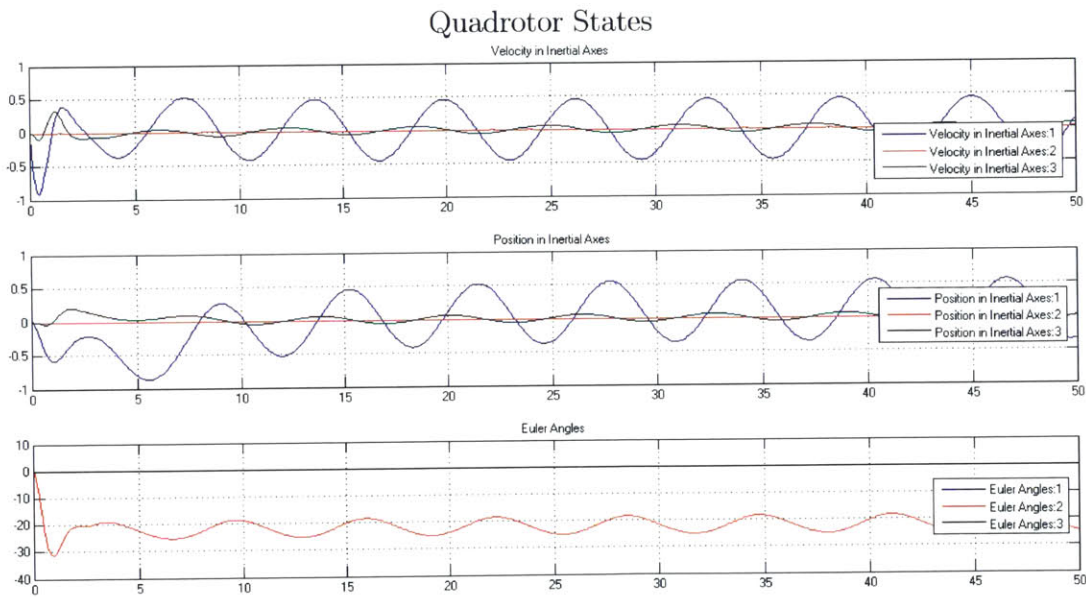


Figure 3-11: Tracking Reference Sine Wave in X-Position at 9 m/s (20 mph)

3.5 Summary

In this chapter, a full system architecture was described. This system uses successive loop closure to control system dynamics matching those described in Chapter 2. An implementation of the system was built and used to analyze the long term dynamics and limitations of the system. This information will be used to inform the experimental design of actual flight tests to be discussed in the following chapters of this thesis.

Chapter 4

Flight Space

This chapter describes the flight testing space created for sustained high speed flight with full state feedback. Flight testing is performed at the Wright Brothers Wind Tunnel at the Massachusetts Institute of Technology [16]. The flight space is equipped with six Vicon motion capture cameras [17] to track the aircraft in real-time, providing pose and velocity information. A picture of the flight space is shown in Figure 4-1. An operation manual for future use of the space can be found in Appendix A.

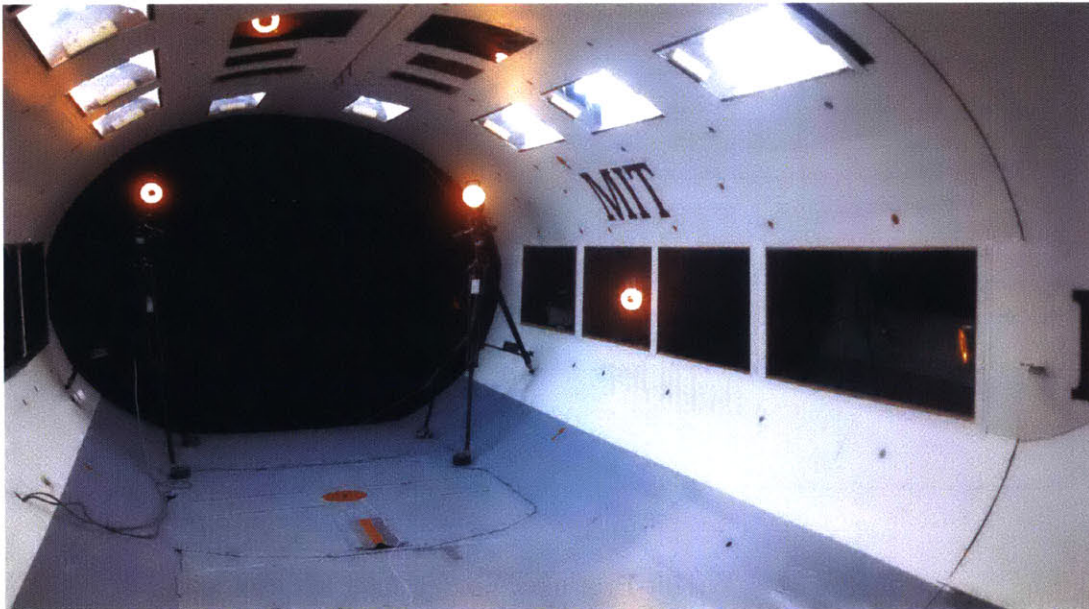


Figure 4-1: Wright Brothers Wind Tunnel Flight Space with Vicon System

4.1 Wind Tunnel

The flight space is located in the Wright Brothers Wind Tunnel at the Massachusetts Institute of Technology. This tunnel is a closed return, closed test section wind tunnel with a 7 foot tall by 10 foot wide elliptical cross section and is 15 feet long. A 2,000 HP AC motor powers the Wright Brothers Wind Tunnel. This motor is capable of running at two constant speeds. and the pitch setting of the fan controls the operating airflow speed. Due to a noise constraint, the tunnel is usually run at the lower speed (up to 90 mph), and only occasionally in second speed (up to 150 mph). This is much faster than any flight tests performed for this work and the more relevant limit is the lowest speed attainable, which is about 10 mph. A diagram of the wind tunnel with relevant information is found in Figure 4-2.

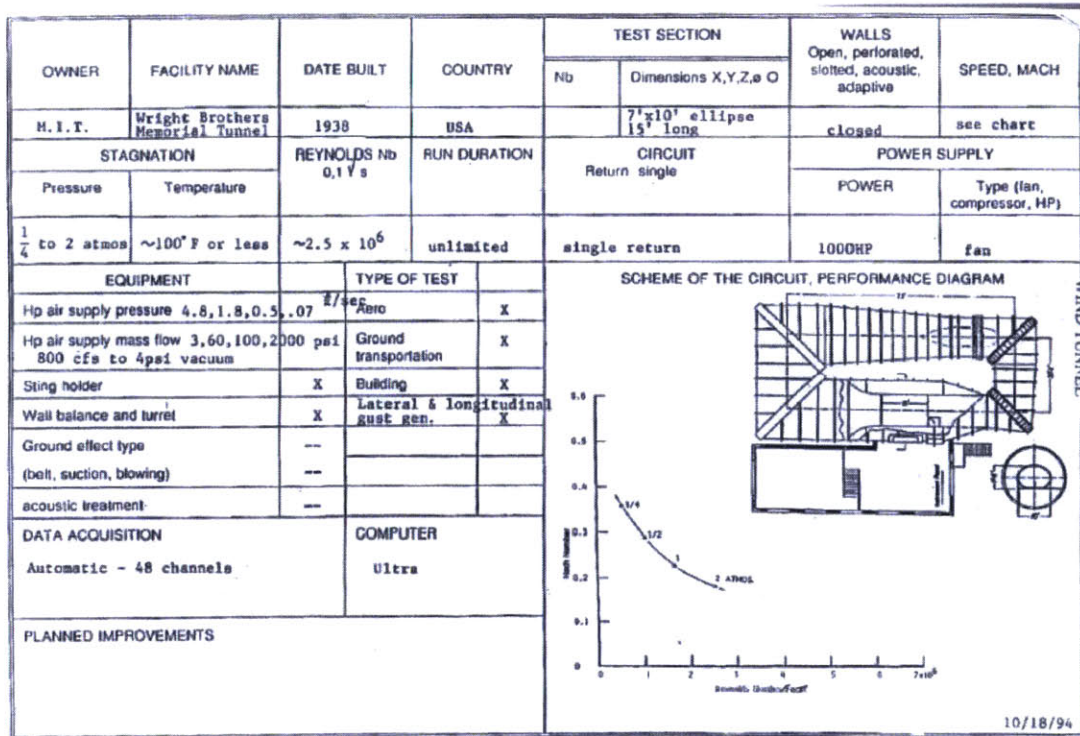


Figure 4-2: Wright Brothers Wind Tunnel Diagram [2]

The wind tunnel is made of several key elements, the wind tunnel shell, the propulsion system, and a set of sensors. The set of sensors installed in the wind tunnel mea-

sure forces and moments on a body installed in the test section. This is the primary use of a wind tunnel, but it is not its purpose for the tests described in this thesis.

Instead of using the wind tunnel to determine aerodynamic properties of an aircraft, it is being used as a proxy for sustained high speed flight. A quadrotor is flown in the wind tunnel to simulate forward flight. To free fly, a different set of sensors are needed both to control the vehicle and to obtain measurements of how the vehicle performs at this flight regime.

4.2 Camera Placement

To allow for full-state feedback and motion tracking to be used for both control and system identification of an aircraft in sustained forward flight, a Vicon motion capture system was integrated into the existing test space within the Wright Brothers Wind Tunnel. A Vicon motion capture system provides real-time pose and velocity information at a rate of 200 Hz. It records groupings of small reflective dots that are rigidly attached to the vehicle being tracked. Images from several cameras are then compared to estimate position, orientation, velocity, and angular rate of the vehicle in 3D space to millimeter precision.

The motion capture system setup in this flight space is comprised of six Vicon motion capture cameras. Four cameras are mounted directly to the exterior of the testing chamber of the wind tunnel. The other two are mounted on tripods as far upstream as possible within the test section. While the tripod mounted cameras are in the freestream, they have no noticeable effect on flight performance as they are far enough upstream that any turbulence they create sufficiently dissipates before reaching the flyable area within the test section. Figure 4-3 is a diagram of the camera placement within the wind tunnel and provides measurements of the flyable area within the test section.

The number and placement of these cameras was heavily constrained by physical limitations in viable mounting locations. Vicon motion capture systems are setup such that the cameras are placed as high up as possible and look down into the space

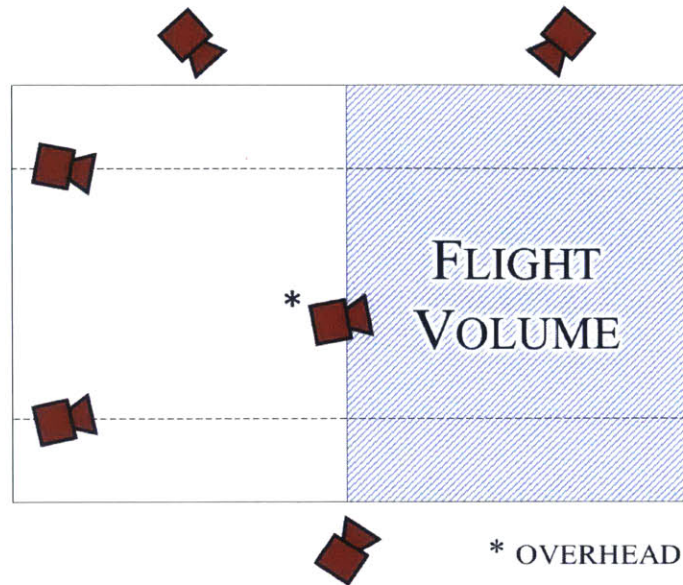


Figure 4-3: Vicon Camera Placement in Wright Brothers Wind Tunnel

they are capturing. This setup is not achievable in the Wright Brothers Wind Tunnel as much of the ceiling of the test section is opaque. There are several windows in the ceiling, but they are close together such that placing multiple multiple cameras in the ceiling provides little more information than if only one camera is placed there.

With only one useful mounting point in the ceiling, the rest of the cameras had to be placed at a lower height and look across the capture space, rather than down onto it. This also led to a new setup constraint as the cameras now see each other resulting in spaces in the capture images of each camera that must be masked, creating blind spots in the sensors. An upper bound on the number of cameras was created by this constraint. For this same reason, a camera is not positioned at the back of the tunnel facing towards the rest of the cameras as images captured by this camera would have blind spots caused by every other camera and it would create a blind spot in images captured by every other camera.

Lastly, an orientation constraint was placed on the cameras. All cameras mounted outside of the wind tunnel test section look through acrylic windows. While Plexiglas does not affect Vicon cameras' ability to capture images, it does reflect the light

given off by the cameras. This reflection can blind the cameras in the same way as described above and often to a greater extent as the reflection creates a much larger blind spot than one created by capturing another camera across the space. Additionally, the cameras are mounted near the windows to maximize the usable space they can capture, which can increase the relative size of a reflection in the capture image. To prevent seeing the reflection, the cameras must be oriented at a large enough angle from the plane of the window such that the reflection is largely out of the capture image.

Given the constraints listed above, cameras were placed in the arrangement shown in Figure 4-3, where the starred camera is the camera mounted in the ceiling. This camera placement covers the entire 7 foot by 10 foot elliptical cross section in an area 8 feet deep resulting in a flyable volume of 440 ft^3 (12.5 m^3) and a footprint of 80 ft^2 (7.4 m^2). Several different aircraft (both fixed-wing and multicopter) have been successfully flown using this setup at speeds up to 30 mph.

4.3 Vehicle Setup

Flying in the Wright Brothers Wind Tunnel with the Vicon setup described in Section 4.2 requires several precautions to increase the reliability of the system and to protect both the wind tunnel and the operators. Taken into consideration is the size of the vehicle, the Vicon dot placement on the vehicle, and flying with a tether.

As stated earlier in this chapter, the test section of the Wright Brothers Wind Tunnel has a ten foot wide by seven foot tall elliptical cross section. While this space is large enough to accommodate all but the largest vehicles used by the Aerospace Controls Laboratory, it does place a size constraint on the vehicles that can be used in the flight space. This constraint is most important when performing lateral maneuvers. The largest aircraft that was flown in the flight space was an Ikarus Yak-54 Shock Flyer [18], a fixed-wing aircraft with a 33 inch wingspan and 31.5 inches in length. The most commonly flown aircraft was a BuddyQuad, a quadrotor developed in MIT's Aerospace Controls Laboratory. The quadrotor is 14 inches across with 8

inch diameter blades and has been flown in lateral maneuvers ± 1.25 meters off of the centerline along the wind tunnel. Figure 4-4 is a size comparison and reference of these two vehicles. The ruler in the picture is a 12 inch ruler.



Figure 4-4: Flight Vehicle Size Reference

As described in Section 4.2, a Vicon motion capture system captures preset groups of reflective dots to track vehicles within its operating space. In order to track both reliably and accurately, all of the tracking dots attached to a vehicle must be clearly visible to at least 3 cameras at all times. The camera placement described in Section 4.2 was chosen to maximize the size of the flight space, but has the drawback of not having a camera placed behind the flight space (reasons for this choice were described in the same section). Thus, in order to maximize the visibility of the Vicon dots, they should be biased towards the front of the vehicle so as to not be blocked by the body of the vehicle, itself. Additionally, mounting the Vicon dots on posts increases their visibility by distancing them from the body of the aircraft and from other Vicon dots. An example dot placement is seen in Figure 4-5, note that most dots are mounted away from the body of the vehicle and those that are close to the body are biased towards the front of the vehicle (marked by the colored tape).



Figure 4-5: Example Vicon Dot Arrangement

In the interest of safety, all flight testing was performed while flying with a lightweight tether. This both protects the pilot of the aircraft if it is flown by hand and serves to prevent damage to the wind tunnel. For the flights to be described in later chapters, the tether is slack during flight and does not affect the dynamics of the vehicle in flight beyond a negligible amount. Some work has been done characterizing flight while the tether is taut [19], but is not discussed in this thesis in detail.

Chapter 5

Hardware and Software

Implementation

This chapter describes the aircraft and flight software used for flight testing in the Wright Brothers Wind Tunnel. First, the aircraft used is described along with its important physical parameters and aerodynamic properties. The software implementation of the control architecture described in Chapter 3 is also detailed.

5.1 Aircraft

The aircraft used for this work is the “BuddyQuad”, a quadrotor designed and manufactured at MIT’s Aerospace Control Laboratory (ACL). A picture of the version of the BuddyQuad used for the flight tests in this thesis is shown in Figure 5-1. This quadrotor was chosen as it is mechanically simple, robust to physical damage, and well-tested and understood using the flight software employed at ACL.

5.1.1 Physical Parameters

The frame of the quadrotor is cut from a single 1/4" sheet of composite material, a carbon fiber and balsa core sandwich. The frame is designed to be lightweight will maintaining rigidity to minimize the vibration issues that commonly hamper



Figure 5-1: The BuddyQuad, a Quadrotor Designed at the Aerospace Controls Lab

quadrotors in flight. The motors, speed controllers and propellers are commercial off-the-shelf (COTS). The quadrotor is flown in the “plus” configuration where the $\hat{\mathbf{b}}_x$ and $\hat{\mathbf{b}}_y$ axes are defined along the arms of the quadrotor. Importantly, the $\hat{\mathbf{b}}_x$, $\hat{\mathbf{b}}_y$, $\hat{\mathbf{b}}_z$ axes are along the principal axes of the aircraft. Thus, the inertia tensor for the aircraft has no cross terms. In other words, the inertia tensor is a diagonal matrix. Additionally, the aircraft is symmetric about the $\hat{\mathbf{b}}_x$ and $\hat{\mathbf{b}}_y$ axes and is radially symmetric in the x-y body plane at intervals of 90° . Therefore, the moments of inertia about the $\hat{\mathbf{b}}_x$ and $\hat{\mathbf{b}}_y$ axes are equal

$$I_x = I_y = I_{xy}.$$

As a result, roll and pitch can be controlled using the same gains and calculating the dynamics is simplified. Values for physical parameters as defined in Chapter 2 for the BuddyQuad are listed in Table 5.1.

5.1.2 Aerodynamic Properties

Unlike quadrotor flight in the hover regime, aerodynamic effects are significant components of the flight dynamics of a quadrotor in sustained forward flight. As described

Table 5.1: Physical Parameters of BuddyQuad

Param	Description	Value	Units
m	Total mass of the vehicle w/ battery	0.416	kg
I_{xy}	Moment of inertia about $\hat{\mathbf{b}}_x$ and $\hat{\mathbf{b}}_y$	0.00417	kg m ²
I_z	Moment of inertia about $\hat{\mathbf{b}}_z$	0.00819	kg m ²
L	Arm length	0.152	m
d	Distance from rotor plane to CoM in $\hat{\mathbf{b}}_z$ direction	0.0254	m
A	Rotor disk area	.0324	m ²

in Chapter 2, there are three major aerodynamics effects that must be accounted for: aerodynamics drag, induced thrust, and blade flapping. Aerodynamic properties needed to calculate these effects were determined for the BuddyQuad using both analytic and experimental approaches and are listed in Table 5.2.

Aerodynamic drag of a quadrotor is difficult to accurately estimate. If the rotors are not powered, the body can be approximated using flat-plate theory. However, this approximation is no longer valid when the rotors are powered because the rotors increase apparent wind and create non-uniform flow over the body, making drag on the entire aircraft difficult to predict. Instead of pursuing an analytic approximation, experimental techniques were used. Using the Wright Brothers Wind Tunnel for its standard purpose, the drag of the BuddyQuad was measured along the body axes, $\hat{\mathbf{b}}_x$, $\hat{\mathbf{b}}_y$ and $\hat{\mathbf{b}}_z$, at velocities from 10-30 mph. Drag constants were calculated from this data (listed in Table 5.2). Note that the standard equation for drag

$$D = \frac{1}{2}\rho C_D S v^2$$

where ρ is the air density, S is the reference area, C_D is the coefficient of drag, and v is the velocity, differs from the drag equations listed in Equation 2.25. The drag constant in the latter equations relates to the former equation with

$$\mathcal{C}_D = \frac{1}{2}\rho S C_D.$$

As stated in Section 5.1.1, the BuddyQuad is radially symmetric in x-y body plane at

intervals of 90° . Thus, the coefficients of drag in the $\hat{\mathbf{b}}_x$ and $\hat{\mathbf{b}}_y$ directions are equal

$$\mathcal{C}_{D,x} = \mathcal{C}_{D,y} = \mathcal{C}_{D,xy}.$$

Experimental results confirmed this relationship.

To calculate the induced thrust and velocity of an actuator disk at a given speed, the induced velocity at hover must be known. This property was calculated analytically using momentum theory, the derivation can be found in Chapter 2. The resulting equation (Equation 2.19) for induced velocity v_h is

$$v_h = \sqrt{\frac{T}{2A\rho}}$$

where T is the thrust generated by the actuator disk, A is the area of the actuator disk, and ρ is the density of air. All three of these values are measurable.

Blade flapping causes the actuator disks on the quadrotor to tip away from the apparent wind generated from velocity in the body x-y plane. A full discussion of this phenomena, its causes and its effects can be found in Chapter 2. The equation (Equation 2.20) for calculating the effect of blade flapping is

$$\alpha = k_f \sqrt{v_x^2 + v_y^2}$$

where α is the angle that the actuator disk rotates off the x-y body plane, k_f is the blade flapping constant, and v_x and v_y are the apparent wind velocity in the $\hat{\mathbf{b}}_x$ and $\hat{\mathbf{b}}_y$ directions, respectively. The blade flapping constant is found experimentally by observing the rotor tilt at known wind velocities. As mentioned in Chapter 2, Blade flapping angle α tends to be on the order of 1° .

5.2 Software

The quadrotor is controlled via a controller using two levels of successive loop closure. This control architecture is identical to that described in Chapter 3 of this thesis and

Table 5.2: Aerodynamic Properties of BuddyQuad

Parameter	Description	Value	Units
$\mathcal{C}_{D,xy}$	Drag constant in $\hat{\mathbf{b}}_x$ and $\hat{\mathbf{b}}_y$.00075	kg/m
$\mathcal{C}_{D,z}$	Drag constant in $\hat{\mathbf{b}}_x$ and $\hat{\mathbf{b}}_y$.00525	kg/m
v_h	Induced velocity at hover	3.48	m/s
k_f	Blade flapping constant	0.01	rad s/m

the software implementation is similar to what is described in Chapter 4 of [13]. The inner loop of the controller is also referred to as the “attitude control loop” and the outer loop is also referred to as the “position control loop”. Reference inputs to the acceleration loop can be set either through direct input (e.g. using a X Box 360™ controller) or from a trajectory planner. The control algorithms used in these two loops are described in Chapter 3. As such, this section instead focuses on the implementation of those algorithms.

5.2.1 Outer Loop

The outer control loop is run off board the aircraft on a separate computer. The function of the position control loop is to output the desired attitude, angular rate, and a total force that will be fed into the attitude control loop. As inputs the outer control loop uses reference position and velocity commands along with measured position and velocity. Reference commands are supplied either via a trajectory planner or through manual commands via an X Box 360™ controller. Position and velocity measurements are supplied from the Vicon motion capture system at a rate of 200 Hz.

The reference and measured values are used to compute a desired linear acceleration in the three directions of the inertial coordinate frame $I (i_x, i_y, i_z)$. The computed accelerations are mapped to desired attitudes, angular rates, and a total force command. The total force command is mapped into a throttle command based on experimental thrust data. These values are sent to the quadrotor over a xBee wireless radio at 100 Hz.

The outer control loop is implemented using the Robot Operation System (ROS) [20]. ROS is an open source software package used for robotics research and development. For this application, ROS handles all of the communication between different segments of the flight software except the wireless communication between the computer and the quadrotor.

5.2.2 Inner Loop

The inner control loop is run on board the aircraft on a custom autopilot named the UberPilot [13]. The function of the attitude control loop is to output the motor commands that will actuate the quadrotor. As inputs the inner control loop uses reference attitude commands, reference angular rates about the body axes of the vehicle (b_x, b_y, b_z), and a total thrust command. These reference values are compared to measured attitude and angular rate values. Attitude measurements are supplied by integrating data from gyros on board and the Vicon motion capture system using a complementary filter. Motion capture data is supplied at a rate of 200 Hz and angular rates are measured with onboard gyros at a rate of 1 kHz. Motor commands are computed to match the reference and measured attitude and angular rate values.

5.2.3 Data Logging

Data is logged while the flight software is running at a rate of 100 Hz. Using ROS, measured and reference values for position, velocity, attitude, angular rates, and throttle commands are all captured. When the flight software closes, flight data is exported to a rosbag file. This file can be imported into several programs, including MATLAB, for analysis, plotting, and simulation.

5.3 Summary

The quadrotor, autopilot, and control software used was all developed at the Aerospace Controls Laboratory. It was chosen because it is robust and well-tested within the

lab. Physical parameters and aerodynamic properties used in the equations of motion derived in Chapter 2 for the BuddyQuad have been measured and calculated.

Chapter 6

Experimental Results

This chapter presents the results of flight testing a quadrotor in forward flight. These tests are used to determine the validity of the model and system described in Chapters 2 & 3 and to perform a system identification of a quadrotor in forward flight.

The structure of the chapter is as follows. First, the experimental design is described. Then the experimental data is compared to the simulated system. Next, the system identification techniques used to analyze the system are reviewed. Finally, a model of the system produced through the system identification is presented.

6.1 Experimental Design

To perform the flight tests, the hardware and software described in Chapter 5 were used to fly a quadrotor in the flight space added to the Wright Brothers Wind Tunnel as discussed in Chapter 4. All test flights followed this basic procedure:

1. With the wind tunnel producing no wind, takeoff and maneuver the quadrotor to the center of the flight space
2. Gradually increase the wind speed to the desired wind speed then allow the quadrotor to settle back to the center of the flight space (reference position). The length of this step was informed by the data in Table 3.1.
3. Log data as governed by the experiment requirements.

4. Gradually decrease the wind speed and land the quadrotor.

Two main sets of experiments were performed to compare to the simulated system from Chapter 3 and to perform and validate the system identification presented in this chapter.

The first set of flight tests involved flying the quadrotor in the wind tunnel while maintaining a constant position. Data from this set of experiments is used to compare the performance of the physical system to that of the simulated system discussed in Chapter 3. Flight data was taken at wind speeds of 10 mph (lowest speed the Wright Brothers Wind Tunnel can run), 15 mph, 20 mph, and 25 mph. Additional flights were performed to determine the maximum wind speed at which the quadrotor could fly.

The second set of flight tests were performed to gather data for a system identification of the quadrotor in forward flight. Similar to the first set of experiments, flight data was taken at wind speeds of 10 mph, 15 mph, 20 mph, and 25 mph. During these flights, a pseudo random input was applied in the x,y, and z inertial directions sequentially to excite the dynamics in each direction. Multiple sets of data were recorded during this set of flight tests to provide separate modeling and validation data.

6.2 Comparison of Physical and Simulated System

A set of flight tests (as described in Section 6.1) were performed in an attempt to match the simulation tests. As it is physically impossible to instantaneously apply a wind force to the quadrotor, both due to wind tunnel operating limitations and the size of the flight space, the rise time and settling time of the system cannot be compared. The simulation results discussed in Section 3.4.3 were instead used to govern experimental design as mentioned in the preceding section. The steady state attitude response of the simulated system and physical system are compared. The operating limits of the two systems are also discussed.

To determine the steady state attitude response, the quadrotor was flown in the

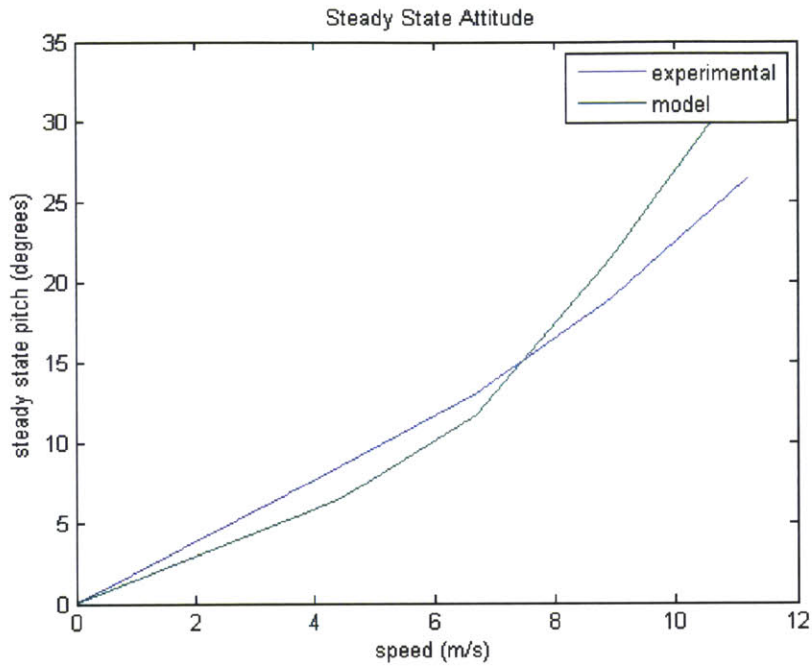


Figure 6-1: Steady State Pitch of the Simulated and Physical Systems as a Function of Wind Speed

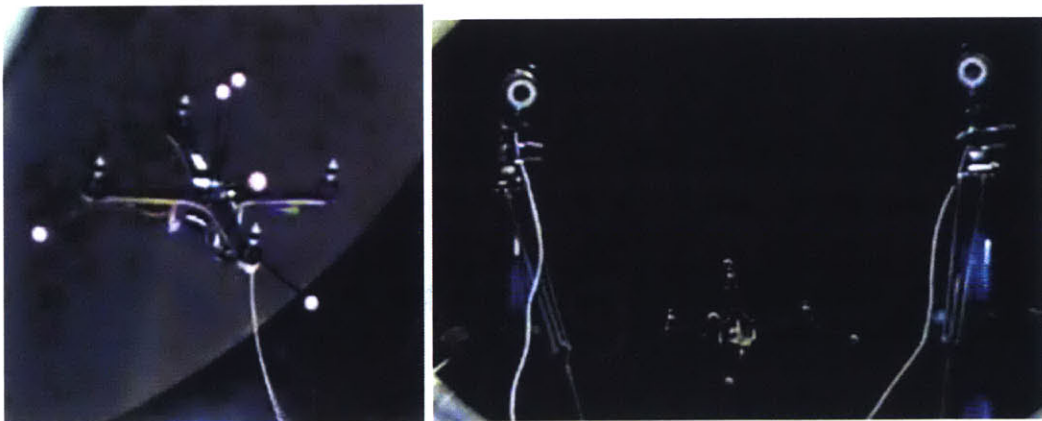


Figure 6-2: BuddyQuad during Flight Testing in Wind Speed of 25 mph

wind tunnel at speeds ranging from 10 to 25 mph while tracking a constant reference position. Similar to the simulated system, the quadrotor is symmetric such that the attitude response in pitch matches the attitude response of the roll with the respective wind speeds applied. Building from Figure 3-7, Figure 6-2 shows the steady-state pitch angle of the quadrotor as a function of wind speed for both the simulated system and the physical system. As predicted in the simulated system, the experimental steady state pitch is related to wind speed via a nonlinear function, specifically a quadratic function. Additionally, the magnitude of the steady-state behavior predicted by the model closely matches the experimental results. The average difference between the steady state pitch of the simulated and physical system is 2.6° .

Additional flight tests were performed to determine the maximum flight speed of the physical quadrotor. The fastest wind speed in which the quadrotor could return to the reference position was 29 mph (compared to the simulated value of 30 mph from Chapter 3). The highest speed at which the quadrotor could follow non-constant reference commands was 27 mph. This speed is equal to the maximum speed at which the simulated system could accurately track a sine wave for the x position reference in Section 3.4.3.

The flight tests performed to validate the model presented in Chapters 2 and 3 suggests that the model accurately simulates the steady state response of actual system along with its operation limits, namely maximum flight speeds for constant position and reference tracking.

6.3 System Identification

To perform a system identification of the quadrotor in forward flight, subspace methods were used for the estimation. This section is a brief overview of subspace methods. This review is largely based on [21]

Any linear system can be represented as

$$x(t+1) = Ax(t) + Bu(t) + w(t) \quad (6.1)$$

$$y(t) = Cx(t) + Du(t) + v(t) \quad (6.2)$$

where $x(t)$ is the state vector, $u(t)$ is the input vector, $y(t)$ is the output vector, $w(t)$ is the process noise and $v(t)$ is the measurement noise. Assuming that $x(t)$, $y(t)$, and $u(t)$ can be measured, form the linear regression

$$Y(t) = \Theta\Psi(t) + \mu(t) \quad (6.3)$$

to estimate Θ where

$$Y(t) = \begin{bmatrix} x(t+1) \\ y(t) \end{bmatrix}, \quad \Theta = \begin{bmatrix} A & B \\ C & D \end{bmatrix}$$

$$\Psi(t) = \begin{bmatrix} x(t) \\ u(t) \end{bmatrix}, \quad \mu(t) = \begin{bmatrix} w(t) \\ v(t) \end{bmatrix}.$$

First the state vector must be estimated using the input data and the output data. Define the system using a finite impulse response (FIR)

$$y(t) = \sum_{j=0}^N [g(j)u(t-j) + h(j)e(t-j)]. \quad (6.4)$$

where $g(j)$ and $h(j)$ are pre-chosen coefficient sequences and $e(j)$ is the innovation. Next, define the k -step ahead predictor

$$\hat{y}(t|t-k) = \sum_{j=k}^N [g(j)u(t-j) + h(j)e(t-j)] \quad (6.5)$$

and

$$\hat{Y}_r = \begin{bmatrix} \hat{y}(t|t-1) \\ \vdots \\ \hat{y}(t+r-1|t-1) \end{bmatrix}, \hat{\mathbf{Y}} = [\hat{Y}_r(1) \ \dots \ \hat{Y}_r(N)]. \quad (6.6)$$

Given this, as ($N \rightarrow \infty$) the linear system has an n th order minimal state space description iff

$$\text{rank}(\hat{\mathbf{Y}}) = n, \forall r \geq n \quad (6.7)$$

The state vector of the minimal realization of the state space can be chosen as a linear combination of $\hat{Y}_r(t)$. This allows us to compute a state vector given the input/output data.

To estimate the k -step ahead predictors, the innovation $e(j)$ can be written as a linear combination of the past input-output data. The predictor is more explicitly written as

$$\hat{y}(t+k-1|t-1) = \theta_k^T H_s(t) + \gamma_k^T G_l(t) + \varepsilon(t+k-1) \quad (6.8)$$

where

$$H_s(t) = \begin{bmatrix} y^t(t-1) & \dots & y^T(t-n_1) & u^T(t-1) & \dots & u^T(t-n_2) \end{bmatrix}^T$$

$$G_l(t) = \begin{bmatrix} u^T(t) & \dots & u^T(t+l+1) \end{bmatrix}.$$

The parameters n_1 and n_2 are chosen and l generally is equal to r . By definition of the k -step predictor, the effect of $G_l(t)$ is ignored such that the k -step predictor is

$$\hat{Y}_r(t) = \hat{\Theta} H_s(t). \quad (6.9)$$

The basic algorithm is as follows

1. Choose n_1, n_2, r , and l . Form \hat{Y}_r and \mathbf{Y} .
2. Estimate the rank of \mathbf{Y} and compute the state vector, $x(t)$,
3. Estimate A, B, C, D and the noise covariance matrices

In practice, there are several ways to implement this algorithm. For the purpose of this thesis, the implementation was completed through the MATLAB System Identification Toolbox [14]. Continuous state-space models of the system were estimated using the subspace (N4SID) method.

6.4 Model for Quadrotor in Forward Flight

Using the methods described in the preceding section, a model for a quadrotor in forward flight was identified. From the system dynamics block, the inputs of the system to be identified are the four thrust forces (F_1, F_2, F_3, F_4) and the wind speed ($u_{cm,rel}$). Note that, due to the symmetry of the quadrotor and limitations of the wind tunnel, the wind speed is always in the negative x direction in the inertial axis. There are twelve outputs to the system, the position vector, the velocity vector, the attitude vector, and the angular rate vector, all of which have three components each. The position vector, velocity vector, and attitude vector are represented in the inertial frame.

Using the experimental design described in Section 6.1, multiple sets of flight data was captured at four wind speeds (10 mph, 15 mph, 20 mph, and 25 mph). The gathered data was divided into two sections, the first was used for the system identification itself. The second set was used as a separate validation set. All data sets are informative and the four thrust force inputs are persistently exciting of order 50. The wind speed input is essentially a constant, so is only persistently exciting of order 1.

The first attempt at system identification involved constructing a single state-space system with 5 inputs and 12 outputs. The model was constructed at several different model orders ranging from 6th to 16th order. Every model built with this structure was highly inaccurate. Figure 6.4 shows examples of the 12th order (default choice using System Identification Toolbox) model output compared to the validation data at 25 mph using this naive model structure. While the velocity in the x and y direction (u and v) eventually converge to the validation data after large transients,

all other states converge to incorrect values.

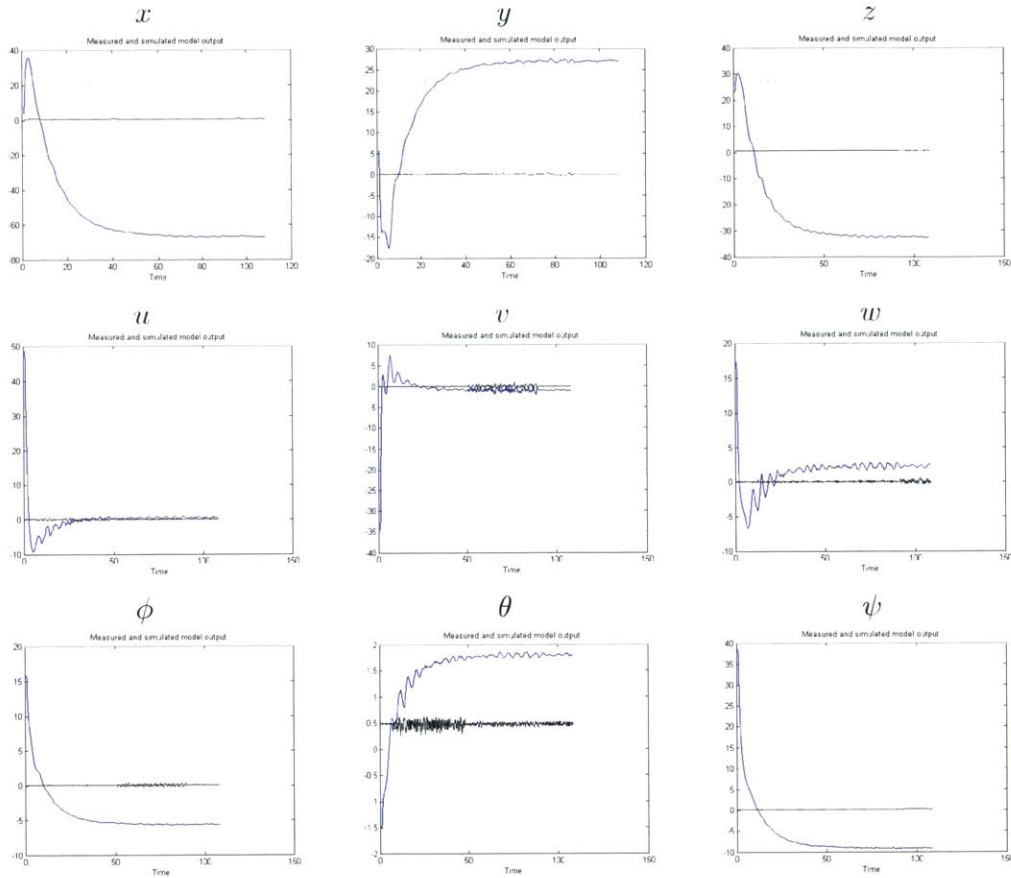


Figure 6-2: Model Output of Single State-Space System Identification Compared to Validation Data at 25 mph (11.2 m/s)

To produce more accurate models without using higher order models, the structure of the model was changed. Instead of a single state-space system relating the five inputs to all twelve outputs, four state-space systems were identified relating the five inputs to each output vector individually. Each output vector is fed back into the inner and outer control loop separately, allowing for this formulation.

Using this model structure, four models were produced at each wind speed that flight tests were performed at (10 mph, 15 mph, 20 mph, and 25 mph). Third and fourth order models were identified using all five inputs. Additionally, third and fourth order models were identified using four inputs, removing the wind speed as an

input. Table 6.1 lists the total error of the model output when compared to a set of validation data of each model type at all operating speeds.

Table 6.1: Total Error of Model Output Compared to Validation Data

Wind Speed = 10 mph (4.5 m/s)

Model		Position (m)			Velocity (m/s)			Attitude (deg)		
order	input	x	y	z	u	v	w	ϕ	θ	ψ
3	4	136	274.7	38.48	12.22	9.156	1.913	64.27	31.17	1336
4	4	28.13	119.7	98.02	4.502	2.219	7.487	40.47	256	1290
3	5	189.4	229.5	58.67	2396	554.4	1255	4.796	75.76	1074
4	5	1.924	86.08	166.5	1082	472.3	681.5	200.1	86.19	985.1

Wind Speed =15 mph (6.7 m/s)

Model		Position (m)			Velocity (m/s)			Attitude (deg)		
order	input	x	y	z	u	v	w	ϕ	θ	ψ
3	4	226.1	25.72	26.79	12.07	367	199	18.97	10.28	81.03
4	4	61.96	122.5	112	86.59	12.27	10.02	11.52	2.6	144
3	5	280.9	28.82	85.48	500.7	312.9	36.73	14.09	48.58	222.6
4	5	185.8	96.8	119.4	1864	1037	219.7	20.48	40.12	133.2

Wind Speed =20 mph (9 m/s)

Model		Position (m)			Velocity (m/s)			Attitude (deg)		
order	input	x	y	z	u	v	w	ϕ	θ	ψ
3	4	17.38	275.3	161.6	179.2	226.3	34.21	25.91	10.29	199.4
4	4	12.57	277.5	144.1	68.46	245.5	27.76	124.3	29.42	917.4
3	5	23.64	283	119.8	163.7	247.9	27.72	34.01	20.3	182.8
4	5	62.77	444.5	776.3	230.8	185	63.38	135.5	4.052	1461

Wind Speed =25 mph (11.2 m/s)

Model		Position (m)			Velocity (m/s)			Attitude (deg)		
order	input	x	y	z	u	v	w	ϕ	θ	ψ
3	4	62.86	363.9	232.4	161.7	4.135	96.43	32.52	10.89	369.7
4	4	26.88	67.97	37.49	148.5	5.271	88.53	32.14	18.4	733.5
3	5	10.83	95.31	131.9	51.92	10.49	55.41	38.86	3.238	87.54
4	5	25.99	102.6	130.9	3.413	4.111	53.83	22.81	17.54	491.1

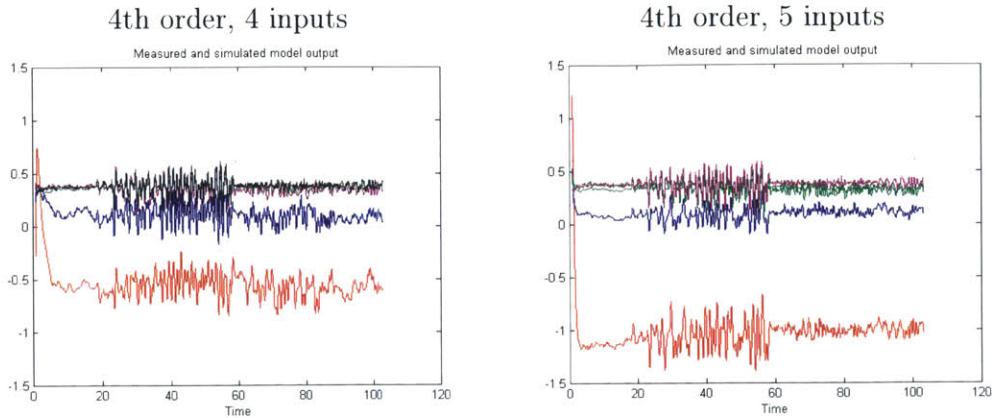
The key points to be gathered from this set of data are

- The 4th order models exhibit overall less total error between the model output and the validation data than the 3rd order models. This shows that the 4th

order models are more accurate than the 3rd order models without overfitting to the testing data.

- At lower wind speeds (10 mph, 15 mph) the 4th order models using 4 inputs exhibit overall less total error than the 4th order models using 5 inputs for all outputs. At higher wind speeds (20 mph, 25 mph) the 4th order models using 5 inputs exhibit overall less total error than the 4th order models using 4 inputs for the velocity outputs but has comparable performance to the 4th order, 4 input models for all other outputs. This is due to the 5th input (wind speed) essentially being a constant resulting in data that does not add any information when estimating the model.
- The 4th order models (both 4 and 5 inputs) exhibit robustness when applied to validation data taken at a slower wind speed than the testing data used to generate the model. When applied to validation data taken at a higher wind speed than the testing data, the models match the shape of the response of the validation data, but at a steady negative bias (shown in Figure 6.4). The bias is larger in magnitude as the difference in wind speeds is larger. The 4th order, 4 input models have a smaller bias than the 4th order, 5 input models. This is unsurprising, as the former models are agnostic to the wind speed.
- For nearly every model at every tested wind speed, the yaw has a large total model output error. This is due to limitations in the experimental setup. During flight, the quadrotor was tethered for safety reasons. This tether was attached to the front of the quadrotor and prevented large changes in yaw ($> 90^\circ$) as it could get tangled in the side rotors especially at high pitch angles.

From this data, the 4th order, 4 input models were chosen as the most promising. These models exhibit less total error than the alternatives and are more robust to errors in wind speed. Figure 6.4 shows the model output of the chosen state-space models compared to validation data. This process gives a set of linear models that can be used to estimate the behavior of a quadrotor in forward flight at different



model estimated at 10 mph (red), model estimated at 15 mph (blue), model estimated at 20 mph (green), model estimated at 25 mph (purple), validation data at 20 mph (black)

Figure 6-3: Model Output for Estimated Pitch Compared to Validation Data at 20 mph (9 m/s)

operating speeds. The models can be used to develop linear controllers for the system that can be scheduled based on forward speed. The state-space systems can also be parameterized with respect to wind speed to simplify the estimated model.

6.5 Summary

Flight testing was performed to analyze the performance and dynamics of a quadrotor in forward flight. This was achieved by controlling a quadrotor in free flight while inside an wind tunnel. Two sets of experiments were run. The first was to analyze the quadrotor flying at a constant forward speed. Data from this set of tests was used to determine the validity of the dynamic model of the system described in Chapter 2. The second set of experiments were performed to gather data to perform and validate a system identification of the quadrotor. The system identification was performed using subspace methods and its accuracy when compared against experimentally gathered validation data was discussed.

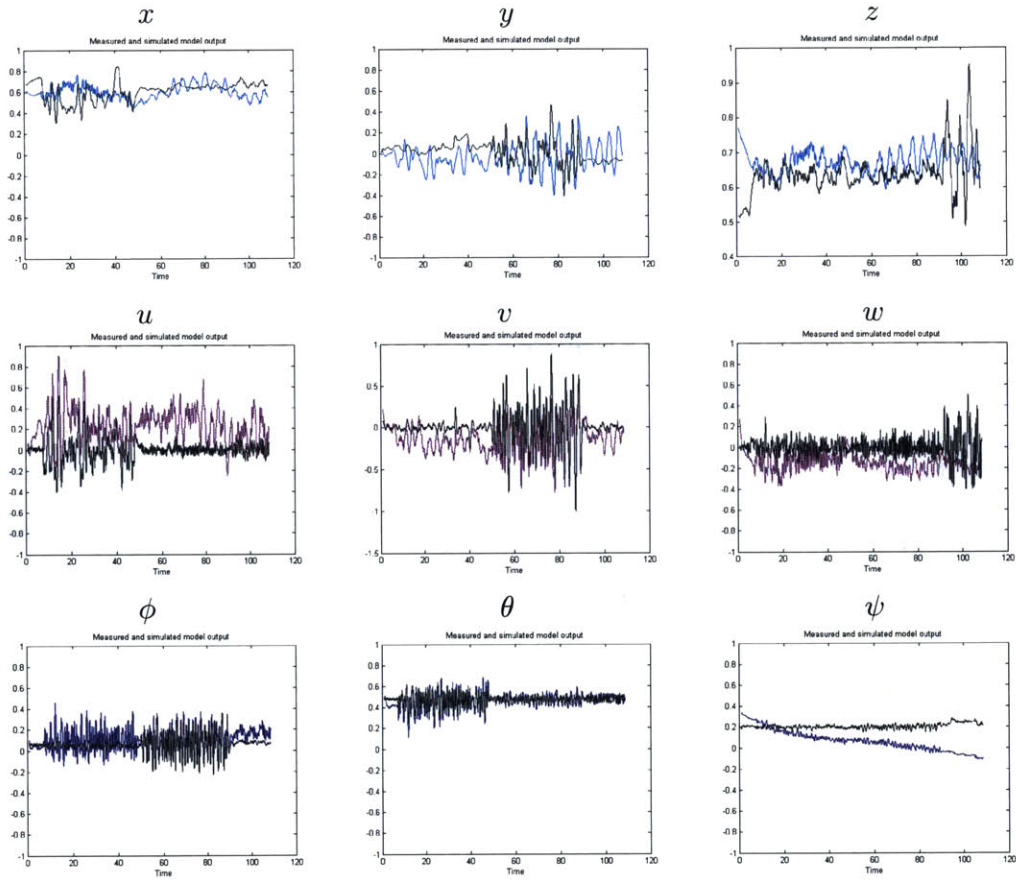


Figure 6-4: Model Output of 4th Order, 4 Input State-Space System Identification Compared to Validation Data at 25 mph (11.2 m/s)

Chapter 7

Conclusion

7.1 Summary

This thesis details the analysis of a quadrotor in forward flight. At high speeds, the aerodynamic effects commonly neglected when modeling quadrotors become important and govern the response of the system. The extent of these effects has been modeled both by a set of nonlinear dynamics that agree with experimental flight data and a set of state-space models created via system identification from flight testing data. The dynamics model presented accurately predicts the steady state performance of the system along with its operating limits. The system identification provides a set of linear models at different operating speeds which could be used to develop control laws for the system. The flight tests which gathered this data were made possible by constructing a new flight space capable of supporting high speed flight.

The main contributions of this thesis are (1) a flight space capable of supporting high speed flight is constructed by augmenting a wind tunnel with a motion capture system (an operation manual for the flight space is provided); (2) a full dynamic model incorporating rigid body dynamics and aerodynamic effects is checked with flight data; and (3) flight experiments are conducted to perform a system identification of a quadrotor in forward flight, providing estimated state-space models for the system at different flight speeds.

Chapter 1 gives an overview of the use of quadrotors in current control research applications. Work on detailed quadrotor modeling is featured with particular emphasis on models including aerodynamic effects.

Chapter 2 provides the derivation of a dynamic model for a quadrotor in sustained forward flight. This model incorporates both the rigid-body dynamics commonly modeled in quadrotor dynamics and aerodynamic effects that become important when flying at high speed. Specifically the effects of aerodynamic drag, blade flapping, and induced thrust are integrated into a model of the quadrotor dynamics.

A system architecture including controller formulation is provided for the system in Chapter 3. The control law presented is not limited to near-hover conditions, which makes it usable for the flight regime being analyzed. The system uses successive loop closure with two control loops to stabilize the system dynamics presented in Chapter 2. Additionally, the full system is simulated using Simulink, the implementation of which is detailed and provided within the chapter. Steady state performance, operating limits, and control performance of the system are then discussed.

Chapter 4 details the design of the new flight space in the Wright Brothers Wind Tunnel. The flight space was created by augmenting the existing test section of the wind tunnel with a Vicon motion capture system. The properties and capabilities of the wind tunnel are briefly overviewed. A particular emphasis on the design and reasoning behind the Vicon camera placement is placed within the chapter. Finally, vehicle setup and limitations while flying in the wind tunnel are given. These considerations include vehicle size, Vicon dot placement, and flying while tethered.

A description of the hardware and software implementation used for the flight tests is detailed in Chapter 5. The quadrotor, autopilot, and flight software are all custom designed and built in the Aerospace Controls Laboratory. Included are tables of the physical and aerodynamic qualities of the test aircraft. The flight software and control implementation is also covered.

Experimental results from flight tests performed in the wind tunnel flight space are presented and analyzed in Chapter 6. The experimental design and challenges are covered. A comparison of the simulated system from Chapter 3 and the performance

of the physical system is discussed. A brief overview of subspace methods for system identification of state-space systems is given. The system identification process is described along with performance results of the final state-space model of the quadrotor in forward flight at various speeds.

7.2 Future Work

Significant future work exists that can further the understanding of the dynamics and control of a quadrotor in forward flight. Although the model presented in Chapter 2 accurately models a quadrotor in free flight, it has several limitations. The first limitation is that the calculation for induced thrust and velocity only holds when the rotor is not in Vortex Ring State, a region of aerodynamic instabilities where momentum theory no longer applies. Specifically this occurs when the quadrotor is descending. Thus, this model would no longer be valid if the quad were attempting to land or perch directly out of a high speed maneuver. Additionally, ground effect, another aerodynamic effect experienced while landing or flying near the ground, is not considered. This effect is difficult to model and highly dependent on the flight environment, but can significantly influence the quadrotor's dynamics. Future work is needed to add or handle these aerodynamic effects in order for this model to hold while the quadrotor is descending or flying within ground effect.

The flight space set up in the Wright Brothers Wind Tunnel provides the ability to perform flight testing in an entirely new flight regime previously impossible to achieve using indoor flight spaces. The current setup, however, is only semi-permanent. The Vicon cameras mounted to the outside of the wind tunnel test section do not affect other users of the wind tunnel and are thus left in place. However, the cameras mounted on tripods inside the test section must be set up and calibrated before every test session and then must be removed at the end. This process is highly inconvenient, can reduce the accuracy and reliability of the Vicon system if calibrated incorrectly, and adds significant set up and tear down time to test sessions. A more permanent solution for the interior cameras is desirable. A renovation of the wind tunnel has been

in discussion recently and incorporating a motion capture system into the updated tunnel would provide the Wright Brothers Wind Tunnel with a unique capability to support the many research groups working on autonomous flight at MIT.

In addition to the BuddyQuad, several other aircraft (including both multirotors and fixed-wing aircraft) have been successfully flown using the new flight space. Other research topics using the wind tunnel have been pursued and discussed including flying a quadrotor with an active tether and modal excitement of a fixed-wing aircraft for educational demonstration purposes. A more direct extension would be to construct a new multirotor aircraft with larger motors, capable of flying at speeds greater than 30 mph.

Finally, future work in control design could be pursued. The state-space models described in Chapter 6 could be used for a gain-scheduled linear control law parameterized using forward speed. The implementation and testing of which could provide insight into the performance of these models and improve control of the quadrotor in forward flight.

Appendix A

Wright Brothers Wind Tunnel Flight Space Operation Manual

This appendix is written as an operating manual for researchers using the flight space installed in the Wright Brothers Wind Tunnel [16]. First, the setup process for the system is described followed by a step-by-step guide of the operation procedure. For the latter part of this manual, operating knowledge of the Aerospace Controls Laboratory flight software is assumed and differences between the procedure used when flying in the RAVEN flight space [22] and the wind tunnel will be detailed. Other flight software can be integrated into the system but is not currently included in the software setup.

A.1 System Setup

The computer and network setup is comprised of two computers (Linux Machine and Windows Machine), a server (Vicon Server), a router, three converter boxes (Vicon Box), and six Vicon cameras (pictured in Figure A-2). Figure A-3 shows the network setup including the cable types used to connect the components of the system. Both the Linux Machine and the Windows Machine are built with network cards. The Ethernet cables used for the network must be plugged into the ports on the network cards not on the motherboards of the respective machines (the latter ports can be

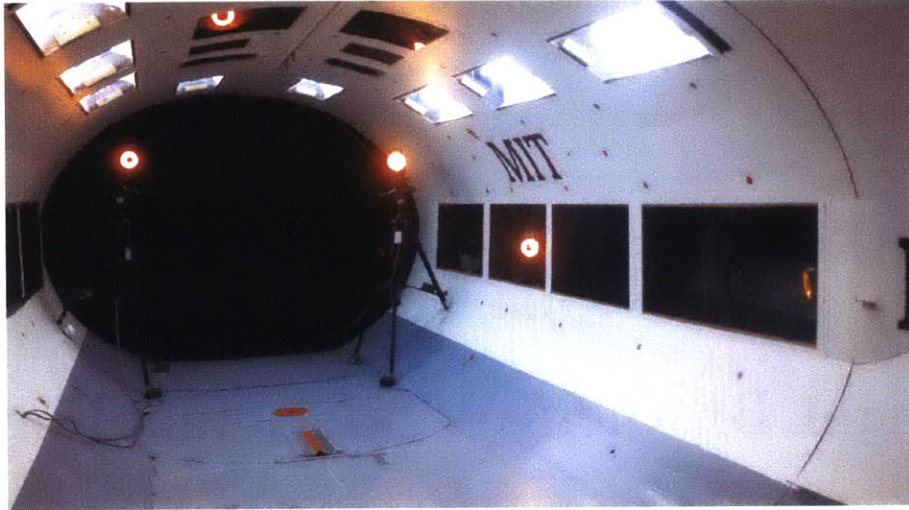
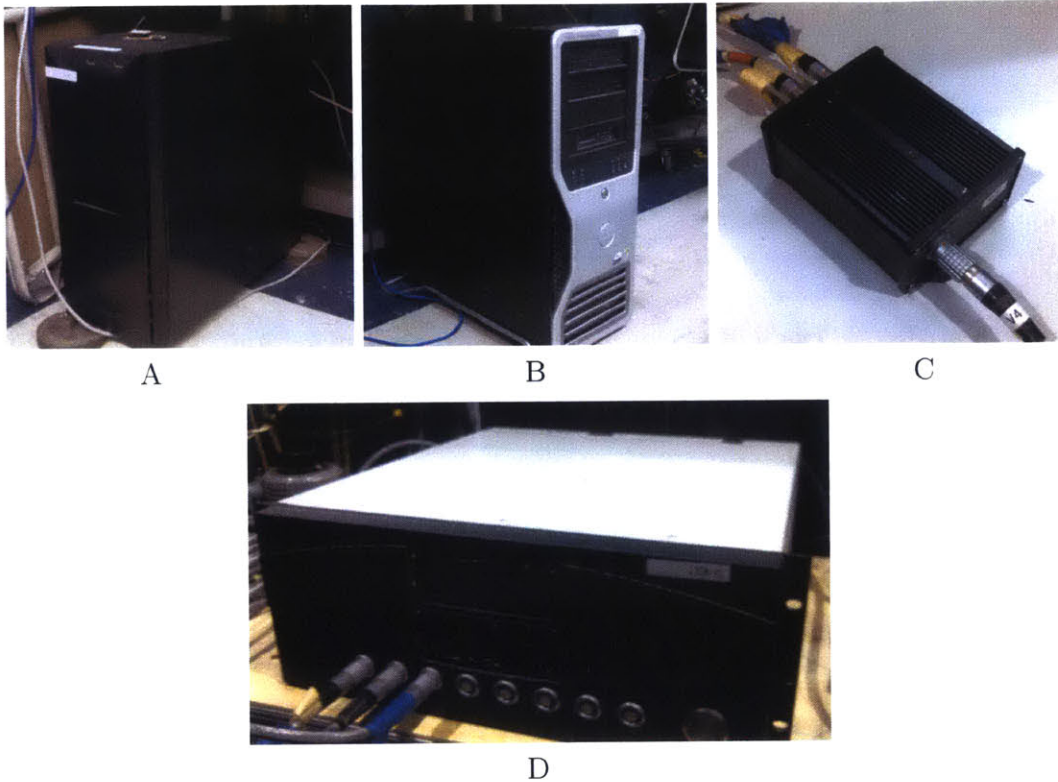


Figure A-1: Wright Brothers Wind Tunnel Flight Space with Vicon System

used for internet connectivity). A USB license key must be plugged into the Windows Machine for the Vicon IQ software to operate correctly. This key is plugged into the back of the Windows Machine and should not be removed for any reason. If the key is missing, please contact the Aerospace Controls Laboratory.

If the Vicon cameras have been removed from the wind tunnel, refer to Figures A-1 & A-4 for camera placement. Two cameras are mounted on tripods and placed within the tunnel during operation. Four more cameras are mounted to the outside of the wind tunnel, two on the far side, one on the near side, and one in the ceiling. In general, the cameras mounted to the outside of the tunnel are relatively permanent fixtures and will not be removed by others using the wind tunnel. The two cameras mounted on tripods and placed within the wind tunnel should be removed as part of the tear down step of operating the flight space. They will have been removed if other groups have used the wind tunnel since the last time the system has been used. Refer to Chapter 4 of this thesis for tips on camera placement if the external cameras have to be reinstalled. Refer to Section A.2 for detailed instructions on setting up the two internal Vicon cameras.



Linux Machine (A), Windows Machine (B), Vicon Box (C), Vicon Server (D)

Figure A-2: Components of the Vicon system in the Wright Brothers Wind Tunnel

A.2 System Operation

This section is a step-by-step guide to operating the Wright Brothers Wind Tunnel flight space. Items referring to the use of non-Vicon software (all software on the Linux Machine) is written using the flight software developed and used by the Aerospace Controls Laboratory.

1. Schedule your time using the Wright Brothers Wind Tunnel:

Before using the flight space, check the current schedule¹ for availability and contact the current AeroAstro staff member in charge of the Wright Brothers Wind Tunnel. At the time of writing this document, the primary operator of the Wright Brothers Wind Tunnel is Richard F. Perdichizzi². This staff

¹<http://aeroastro.mit.edu/about/reserve/wbwt>

²dickp@mit.edu, (617) 253-4924

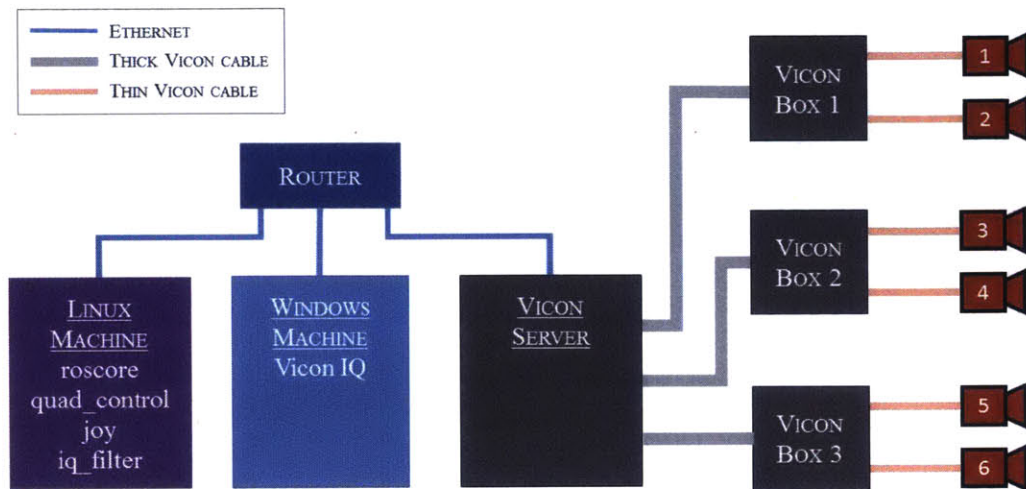


Figure A-3: Network Setup for Flight Space

member is also responsible for running the wind tunnel during flight testing. It is recommended to perform this step as far in advance as possible as the wind tunnel is a shared resource. It is used by students and industry alike and can often be reserved for weeks at a time.

2. Setup the Vicon cameras placed inside the test chamber.

As mentioned in Section A.1, the two cameras mounted on tripods and placed within the test chamber will not be setup if the tunnel has been used by another party. Follow the diagram in Figure A-4 for the position and facing of these two cameras, placing the cameras as far upstream as possible within the test section. The test section shown is 10 feet wide by 15 feet long. The blue shaded area corresponding to the usable flight space is 10 feet wide by 8 feet long. The tripods should be setup with two long legs on the floor of the tunnel and one short leg on the wall of the tunnel (see Figure A-5) to keep as much of the airflow of the tunnel clear as possible. There are various weights in the Wright Brothers Wind Tunnel operating room that can be used to weigh down the tripods for improved stability. The weights used in Figure A-5 are 500 grams each and are placed downstream of the feet on the floor of the wind tunnel and

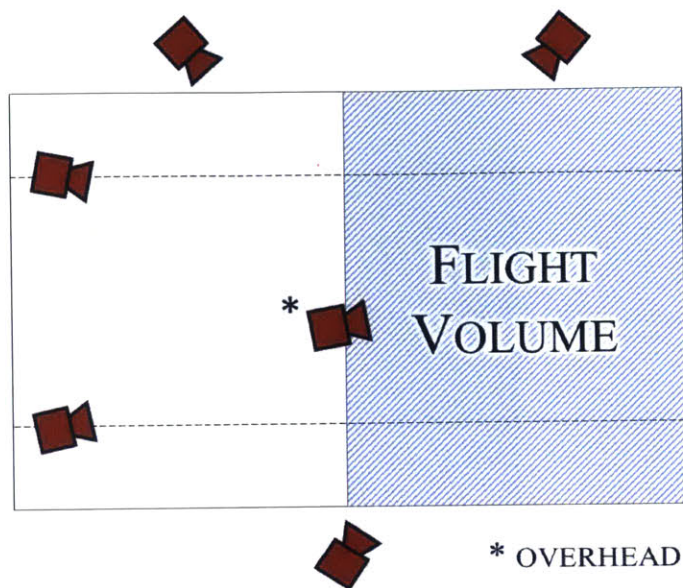


Figure A-4: Vicon Camera Placement in Wright Brothers Wind Tunnel

one is placed on the front side of the center brace of the tripod. The upper section of one of the tripods can be raised to vary the height of the two cameras for additional variance in camera facing. Run the two free thin Vicon cables into the tunnel and connect them using the plug on the back of the cameras. Note that the plugs have a particular orientation. Line up the red dot on the cable and the plug to connect the cameras. To feed the cables into the test section, there is a hole in the left wall of the tunnel (facing upstream) that can be used for this purpose. The two internal cameras should now be connected to the Vicon server via a Vicon converter box.

3. Start and connect to the Vicon motion capture system.

To start and use the Vicon system, first turn on the Vicon server by pushing the large circular button on front of the server. Let the server go through its start up process for about a minute before proceeding. Next, log into the Windows Machine and start Vicon IQ (Start -> Programs/Vicon/Vicon iQ 2.5/VICONiQ 2.5). Click the Setup tab at the top of the window. The menu bar will now include a drop down menu labeled "RealTime Engine". Click it and



Figure A-5: Example Tripod Setup Within Test Section

select "Connect to System". A terminal window will open in the background when the system connects. At the bottom left corner of the screen it will say "RealTime Connected".

4. **Calibrate the Vicon motion capture system.**

The next step is to calibrate the Vicon system. This must be done every time any of the Vicon cameras have been moved or reinstalled. First remove all Vicon dots or objects to be tracked from within the flight space. When the flight space is clear, click into the Setup tab in the Vicon IQ software. In this tab, masks can be created and applied to the cameras to block out errant measurements from reflective surfaces, lights, other cameras, and other sources. On the right side of the window, click "Start Recording Background", wait a few seconds, and then click "Stop Recording Background" (same button). Click "Save Masks and Apply". The software will automatically create and apply masks to the Vicon cameras. The masks on each individual camera can be seen and edited manually in the software but the automatic mask creation tends to be more

effective.

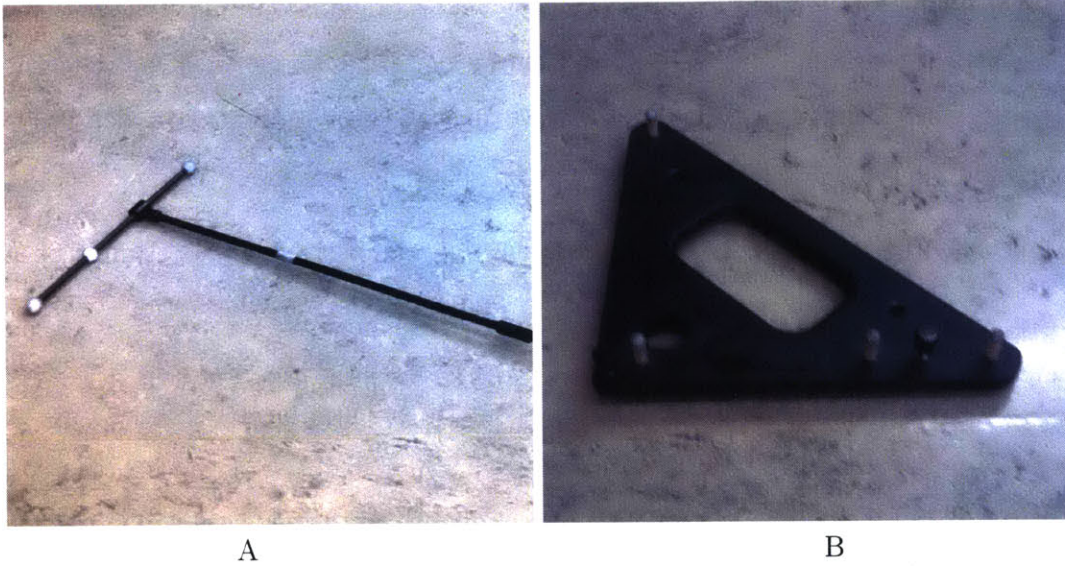


Figure A-6: Vicon System Calibration Tools

Next click into the Calibrate tab. In this step, the cameras will be calibrated using the calibration wand (Figure A-6, A). On the right side of the Vicon IQ software, select "240_mm_Wand" and "Full Calibration" as the options and then click "Start Wand Wave". Go into the flight space with the calibration wand and wave it around making sure that every camera sees you clearly for at least a minute. No particular pattern is required for this step but the resulting calibration is more accurate if the wand is in clear sight of multiple cameras while it is being waved. The Status Report in the lower right corner of the Vicon IQ window displays the number of wands measurements that have been taken during the calibration. For a good calibration, at least 2000 measurements should be taken for each camera, the number will turn green when the software thinks it has enough. Note that certain cameras will have more measurements than others. This is okay as long as all cameras exceed the minimum suggested measurement count. Click "Stop Wand Wave" (same button) and the system will calibrate itself, giving a projection error and status for each camera (this step may take a couple of minutes to complete). At least 5 of 6 cameras being

rated "Excellent" or "Awesome!" is a good calibration and all cameras should at least be rated "Good". If the resulting calibration does not meet these criteria, repeat the wand wave step of the calibration. Focus on cameras that had fewer measurements than other cameras during the prior calibration and/or collect more measurements for all cameras.

Once the cameras have been calibrated, the volume origin and axes must be set. In the Vicon Software, select "Ergo_9mm_LFrame" as the option. Take the LFrame (Figure A-6, B) and place it near the middle of the flight space. The position does not have to be precise, but the orientation does. See Figure A-7 for an example origin placement taking special note of the LFrame's orientation. Make sure that the LFrame is properly aligned to the wind tunnel and is level. The feet of the LFrame can be adjusted to level out the LFrame and it also has levels built into it. Failure to do this will result in inaccurate inertial measurements during operation. In the Vicon software, click "Track L Frame", wait a few seconds, and then click "Set Origin". The volume origin and axes will now be set. Remove the LFrame from the flight space. The Vicon system is now calibrated and ready for objects to be created and tracked.

5. Prepare the aircraft and hardware for flight.

During this step, an object corresponding to the aircraft to be flown will be added to the Vicon tracker. First, place the aircraft to be tracked in the flight space with the front of the vehicle pointing upstream. Similar to the LFrame, the orientation of the vehicle is important and must match the expected inertial axes for accurate tracking. In the Vicon IQ software, click on the Capture tab. Here, an object will be created for the Vicon system to track. The vehicle to be tracked must be equipped with Vicon dots(preferably following the guidelines described in Section 4.3 in this thesis). To create an object, click on the "Create/Edit Objects" tab on the far right of the window. Then click "Begin Editing". Control+left click on the dots corresponding to your vehicle in the Live 3D Workspace. When all the dots have been selected, enter the name of the vehicle

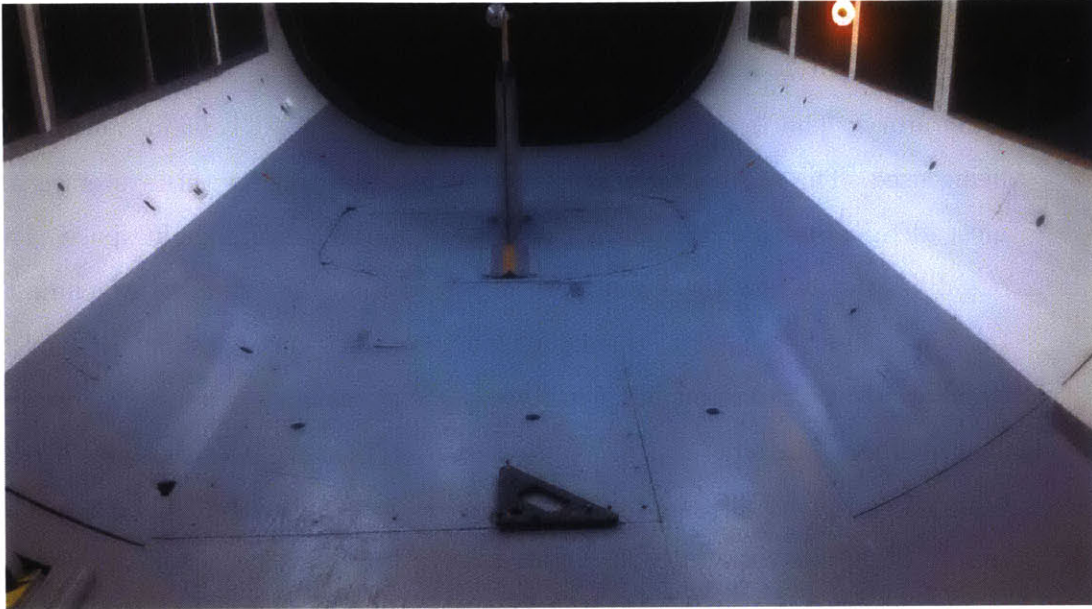


Figure A-7: Set Volume Origin Example (Camera Facing Upwind)

(if using the ACL flight software name must match its corresponding param file), click "Create Object" then "Save and Apply". Click the "Active Objects" tab and confirm that the box next to the name of your object is checked. Physically move the object around in the flight space to check if the object is tracking properly.

Flights should be performed using a tether. The tether protects both the operator if they are within the tunnel and the tunnel itself. For the flight tests described in this thesis, nylon kite string was sufficient material for the tether. In the floor of the tunnel there is a mounting point for a force balance. At that mounting point, a bolt can be raised in the floor. Ask the wind tunnel operator before doing this. Tie a loop in one end of the tether and loop it around the raised bolt and tighten the bolt down to secure the tether to the floor. Attach the other end of the tether to the vehicle. The vehicle is now being tracked by the Vicon software and is ready to be flown safely.

6. Run the flight software on the Linux Machine.

This step details the use of the flight software. Note that this step may vary if using flight software that is different from that used by the Aerospace Controls Laboratory. The rest of this step is written as if the ACL flight software is being used. The procedure of running the flight software for this system is almost identical to that of running the software in the RAVEN flight space. The one difference is how the Vicon data is passed from the Windows Machine to the Linux Machine. After starting `roscore` on the Linux Machine, instead of running a ROTracker on the Windows Machine, open a new terminal window on the Linux Machine and run `roslaunch iq iq_filter_linux`. Upon execution, this script will pass Vicon data of any objects currently being tracked in the Vicon IQ software to ROS on the Linux Machine. The script will close if no objects are currently being tracked or all objects become untracked during operation. Proceed with running the flight software as normal after this point.

7. Perform flights in the Wright Brothers Wind Tunnel.

The flight space is now setup and operational. Flight tests may now be performed using the wind tunnel. As mentioned at the start of the section, the AeroAstro staff member in charge of the Wright Brothers Wind Tunnel is required to run the tunnel. Work with them to run the tunnel as required by your application. If manually piloting a vehicle within the wind tunnel, ear and eye protection are required (both are available in the operating room).

8. Clean up the system and prepare the wind tunnel for the next users.

If you have reserved the wind tunnel for the next session and plan on being the next person using the wind tunnel, confirm this with the staff member and just turn off the Vicon Server and leave the interior cameras set up. This allows the camera setup, Vicon calibration, and object creation steps to be skipped next time, saving a significant amount of setup time. If you do not plan to be the next person using the tunnel, the interior cameras must be removed from the wind tunnel. Turn off the Vicon Server, then disconnect the thin Vicon cables connected to the interior cameras from the back of said cameras. The cameras

do not have to be removed from the tripods. Pack up the tripod and bring them back into the operating room for storage. Run the cables out of the tunnel and spool them near the Vicon Server. Remove the tether from the wind tunnel. If the session was being recorded, you can ask the staff member to finalize the disk for you. Close the Vicon software on the Windows Machine and close all terminals on the Linux Machine.

Bibliography

- [1] D. A. P. Nitin Sydney, Brendan Smyth, “Dynamic control of autonomous quadrotor flight in an estimated wind field,” in *IEEE Conference on Decision and Control*, 2013.
- [2] E. E. Covert and T. Wilson, *A Student’s Introduction to the Wright Brothers Wind Tunnel at MIT*. Massachusetts Institute of Technology, Cambridge, MA, 1 ed., 2004.
- [3] N. K. Ure, S. Omidshafiei, T. B. L. and Ali-akbar Agha-mohammadi, J. P. How, and John Vian, “Heterogeneous Multiagent Learning with Applications to Forest Fire Management,” in *IEEE International Conference on Robotics and Automation (ICRA)*, 2015 (Submitted).
- [4] A. akbar Agha-mohammadi, N. K. Ure, J. P. How, and J. Vian, “Health aware stochastic planning for persistent package delivery missions using quadrotors,” in *IEEE/RSJ International Conference on Intelligent Robots and Systems (IROS)*, 2014.
- [5] DARPA, “Fast lightweight autonomy (fla).” Online, June 2015. http://www.darpa.mil/Our_Work/DSO/Programs/Fast_Lightweight_Autonomy_%28FLA%29.aspx.
- [6] E. Altug, J. Ostrowski, and R. Mahony, “Control of a quadrotor helicopter using visual feedback,” in *Robotics and Automation, 2002. Proceedings. ICRA ’02. IEEE International Conference on*, vol. 1, pp. 72–77 vol.1, 2002.
- [7] B. Zhu and W. Huo, “Trajectory linearization control for a quadrotor helicopter,” in *Control and Automation (ICCA), 2010 8th IEEE International Conference on*, pp. 34–39, June 2010.
- [8] D. Lee, H. Jin Kim, and S. Sastry, “Feedback linearization vs. adaptive sliding mode control for a quadrotor helicopter,” *International Journal of Control, Automation and Systems*, vol. 7, no. 3, pp. 419–428, 2009.
- [9] H. Voos, “Nonlinear control of a quadrotor micro-uav using feedback-linearization,” in *Mechatronics, 2009. ICM 2009. IEEE International Conference on*, pp. 1–6, April 2009.

- [10] G. M. Hoffmann, H. Huang, S. L. Wasl, and E. C. J. Tomlin, "Quadrotor helicopter flight dynamics and control: Theory and experiment," in *In Proc. of the AIAA Guidance, Navigation, and Control Conference*, 2007.
- [11] M. Orsag and S. Bogdan, *Influence of Forward and Descent Flight on Quadrotor Dynamics*, chapter 7, pp. 10–119. Recent Advances in Aircraft Technology, Rijeka, Croatia: InTech, second ed., feb 2012. Matko Orsag and Stjepan Bogdan (2012). Influence of Forward and Descent Flight on Quadrotor Dynamics, Recent Advances in Aircraft Technology, Dr. Ramesh Agarwal (Ed.), ISBN: 978-953-51-0150-5, InTech, DOI: 10.5772/37438. Available from: <http://www.intechopen.com/books/recent-advances-in-aircraft-technology/influence-of-forward-and-descent-flight-on-quadrotor-dynamics>.
- [12] J. G. Leishman, *Principles of Helicopter Aerodynamics*. Cambridge University Press, 2000.
- [13] M. Cutler, "Design and control of an autonomous variable-pitch quadrotor helicopter," master's project, Massachusetts Institute of Technology, Dept. of Aeronautics and Astronautics, Sept. 2012.
- [14] I. The Mathworks, "Matlab and simulink 2014b." Natick, MA, June 2015.
- [15] F. Markley, "Fast quaternion attitude estimation from two vector measurements," in *Journal of Guidance, Control, and Dynamics*, vol. 25, pp. 411–414, 2002.
- [16] D. of Aeronautics and Astronautics, *Wright Brothers Wind Tunnel*. Massachusetts Institute of Technology, Cambridge, MA, 4 ed., 2002.
- [17] T. rep., "Motion capture systems from vicon." Online, June 2015. <http://www.vicon.com/>.
- [18] IKARUS, "Shockflyer." Online, June 2015. <http://shop.ikarus.net/en/63-shockflyer>.
- [19] J. Wiken, "Tethered flight in high-wind environments." Online, Jan. 2015. <http://acl.mit.edu/projects/tetheredFlight.html>.
- [20] ROS, "About ros." Online, June 2015. <http://www.ros.org/about-ros/>.
- [21] J. Songsiri, "Subspace methods." Lecture Notes for EE531, Chulalongkorn University, Bangkok, Thailand, 2010.
- [22] J. P. How, J. Teo, and B. Michini, "Adaptive flight control experiments using RAVEN," in *Proceedings of 14th Yale Workshop on Adaptive and Learning Systems*, (New Haven, CT), pp. 205 – 210, June 2008.